Plasmonic Photoconductors for Higher Performance Terahertz Radiation Sources

by

Christopher William Berry

A dissertation submitted in partial fulfillment
of the requirements for the degree of
Doctor of Philosophy
(Electrical Engineering)
in the University of Michigan
2013

Doctoral Committee:

Assistant Professor Mona Jarrahi, Chair
Assistant Professor Hui Deng
Professor Theodore B. Norris
Adjunct Professor John F. Whitaker

Dedicated to David and Sharon Berry

ACKNOWLEDGEMENTS

I would like to thank all those who helped me reach this point. Foremost, I would like to express my deepest gratitude to my advisor, Professor Mona Jarrahi, for her mentorship. My successes in research are owed to her insightful guidance and patient instruction. Her ability to see a solution around seemingly any problem is enviable, and when progress seemed difficult, I was inspired by her resolve. Her kindness and magnetic personality have made it a pleasure to work with her.

I would also like to thank the members for my dissertation committee, Professor Hui Deng, Professor Theodore Norris, and Professor John Whitaker, for their support and invaluable advice. In my time at the Michigan, I depended on the help of many friends. First, I would like to thank the members of my research group. A special thanks to Dr. Mohammed Reza Hashemi for trying his best to teach a slow learner about all things RF and to Professor Mehmet Ünlü for freely sharing his extensive experience with me. I would like to thank Ning Wang for all her help in the lab and with device physics. I would like to thank Shang-Hua Yang for all his help in the cleanroom, lab, and for making the best coffee on North Campus. Thanks to Nezih Tolga Yardimci for his helpful discussions.

Additionally, I am indebted to Jeremy Moore for his training in both the cleanroom and in the lab. I would like to thank Dr. Chi-Sen Lee for sharing his knowledge of fabrication and his many hours of help. Finally, I would like to thank the staff and friends in the Radiation Laboratory and the LNF for their tremendous help.

TABLE OF CONTENTS

LIST OF FIGURES

Figure

LIST OF APPENDICES

Appendix

CHAPTER I

Introduction

The terahertz (THz) frequency range lies in the electromagnetic spectrum between the microwave and optical regions, as shown in Fig. 1.1. A wide variety of light and heavy molecules have rotational and vibrational resonances in the terahertz frequency range [1]. Due to these transitions, it has been estimated that approximately 98% of all photons emitted since the Big Bang fall in the 1-8 THz frequency range [2]. Therefore, spectroscopic analysis of the terahertz radiation emitted from interstellar dust clouds gives a window into understanding the early Universe [3]. Additionally, terahertz spectroscopy is employed for a variety of applications including bio-sensing [4–6], chemical sensing [7], environmental monitoring [8, 9], material characterization [10], and explosive detection [8].

In addition to spectroscopic applications, terahertz technology is finding an increasing demand in imaging. Generally, the resolution of an optimized imaging system is approximately equal to the wavelength of operation, which for terahertz radiation allows for sub-millimeter imaging resolution. Near-field imaging techniques have been shown to further improve image resolution to sub-micron scales [11]. In contrast to X-rays, terahertz radiation is non-ionizing and nondestructive, making it an attractive solution for medical imaging such as in detection of breast cancer [12], skin cancer [13], and tooth decay [14, 15]. Additionally, due to its transparency to otherwise opaque packaging materials such as wood, plastic, and cloth, terahertz waves are finding increasing application in security screening [16], pharmaceuticals [17], and quality control [18].

Although this region has been of great scientific interest since the 1920s [19], it has only recently become technologically accessible. Advances in optical sources, microwave technology, and nanofabrication have spurred the growth in terahertz technology. Compared to the capabilities of optical or microwave devices, however, terahertz technology is currently underdeveloped. In this dissertation, I will focus on improving sources of terahertz waves.

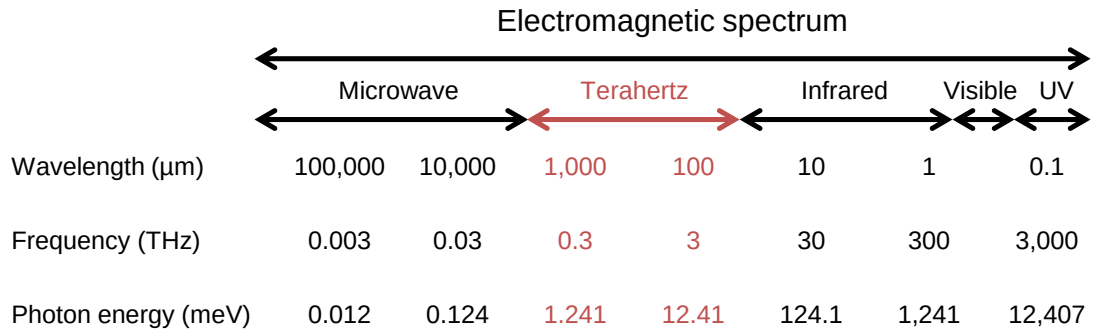

Figure 1.1: The regions of the electromagnetic spectrum surrounding the terahertz range.

1.1 Overview of Terahertz Sources

To realize high performance terahertz radiation sources, there has been a great deal of effort in extending the high frequency limit of RF sources, in minimizing the low frequency limit of optical emitters, and in combining RF and optical techniques [8]. From the RF side, IMPATT diodes, Gunn diodes, resonance tunneling diodes [20, 21], and chains of frequency multipliers [22, 23] have demonstrated very promising compact terahertz sources. However, this category of sources has limited bandwidth, poor power efficiency, and low output power levels. On the other hand, electron beam devices such as backward wave oscillators [24] and traveling wave tube regenerative amplifiers [25] can produce reasonable power levels, but their operation has not been demonstrated above 1.5 THz [26]. Additionally, the bulky nature of backward wave oscillators and their requirement for high magnetic fields and vacuum limits their use

in various operational settings.

From the optical side, quantum-cascade lasers have been under an extensive investigation during the past decade [27]. Significant progress has been made pushing their operation frequency to 1 THz [28] and their operation temperature to ∼200 K for a 3.22 THz lasing frequency [29]. Additionally, optical down-conversion to terahertz frequencies based on nonlinear optical effects has been extensively used for generating high power terahertz waves. Optical down-conversion to terahertz frequencies in bulk nonlinear materials is inherently inefficient due to the optical/terahertz phase mismatch limiting the efficient field interaction length [30]. Guided wave nonlinear media [31], quasi-phase-matching in periodically poled media [32, 33], and the use of tilted wave-front pump waves [34] have been employed to offer a better phase-matching control, resulting in longer field interaction lengths. However, because of material absorption, the active length in which THz waves are generated is limited to centimeter ranges. Because of the field interaction length limitations, the use of high-power optical pumps has been necessary to provide ultra-high peak powers for generating meaningful terahertz powers using nonlinear optical techniques. An additional inherent limitation of nonlinear optical techniques for generating terahertz waves stems from the conservation of energy in a nonlinear optical process, namely the Manley-Rowe rule [35]. In other words, the maximum power efficiency of terahertz sources based on nonlinear optical phenomena is limited to the ratio between the energies of the generated terahertz photon and the pump optical photon.

On the other hand, optical-to-terahertz conversion through photoconduction has demonstrated very promising performance [36–42] and has been the most commonly used technique for generating terahertz waves since the pioneering demonstration of picosecond photoconducting Hertzian dipoles in 1984 [43]. One of the main advantages of photoconductive terahertz emitters compared with the terahertz emitters based on nonlinear optical phenomena is that their power efficiency is not restricted

by the Manley-Rowe limit. This is because one electron-hole pair can be generated for each absorbing photon, which can emit several terahertz photons on reaching the terahertz antenna in a photoconductive emitter. In other words, the optical-to-terahertz conversion efficiency of photoconductive terahertz emitters can reach 100%, orders of magnitude higher than the Manley-Rowe limit. Although the optical-to-terahertz conversion efficiency of photoconductive emitters can theoretically reach 100%, the low-quantum efficiency of conventional ultrafast photoconductors imposes substantially lower conversion efficiencies. This dissertation details a new architecture for improving the optical-to-terahertz conversion efficiency of photoconductive terahertz sources by incorporating plasmonic contact electrodes.

1.2 Organization of the Dissertation

This dissertation is organized as follows.

Chapter II gives an introduction to photoconductive terahertz sources. Impedance matching is considered for both symmetrically excited and asymmetrically excited photoconductive sources. The theoretical description detailed in this chapter appeared in the *Journal of Infrared, Millimeter, and Terahertz Waves* [44].

Chapter III introduces photoconductive terahertz sources having plasmonic electrodes. Sections of this chapter appeared in *Nature Communications* [45], the *Journal of Visualized Experiments* [46], and the *New Journal of Physics* [47].

Chapter IV summarizes the main results.

References

[1] T. G. Phillips and J. Keene, "Submillimeter astronomy", *Proceedings of the IEEE*, vol. 80, pp. 1662–1678, 1992.

[2] D. Leisawitz, W. Danchi, M. DiPirro, L. D. Feinberg, D. Gezari, M. Hagopian, J. C. Mather, S. H. Moseley, R. F. Silverberg, W. D. Langer, M. Shao, M. R.

Swain, H. W. Yorke, J. Staguhn, and X. Zhang, "Far-IR/submillimeter space interferometry: scientific motivation and technology requirements", in *2001 IEEE Aerospace Conference Proceedings*. 2001, vol. 4, pp. 4/1995–4/2004, IEEE.

[3] P. H. Siegel, "Terahertz Technology", *Jet Propulsion*, vol. 50, no. 3, pp. 910–928, 2002.

[4] L. Van Zandt and V. Saxena, "Millimeter-microwave spectrum of DNA: Six predictions for spectroscopy", *Physical Review A*, vol. 39, no. 5, pp. 2672–2674, Mar. 1989.

[5] P. Siegel, "Terahertz Technology in Biology and Medicine", *IEEE Transactions on Microwave Theory and Techniques*, vol. 52, no. 10, pp. 2438–2447, Oct. 2004.

[6] M. Nagel, M. Först, and H. Kurz, "THz biosensing devices: fundamentals and technology", *Journal of Physics: Condensed Matter*, vol. 18, no. 18, pp. S601–S618, May 2006.

[7] M. Walther, B. M. Fischer, A. Ortner, A. Bitzer, A. Thoman, and H. Helm, "Chemical sensing and imaging with pulsed terahertz radiation.", *Analytical and bioanalytical chemistry*, vol. 397, no. 3, pp. 1009–17, June 2010.

[8] M. Tonouchi, "Cutting-edge terahertz technology", *Nature Photonics*, vol. 1, no. 2, pp. 97–105, Feb. 2007.

[9] D. Van der Weide, J. Murakowski, and F. Keilmann, "Gas-absorption spectroscopy with electronic terahertz techniques", *IEEE Transactions on Microwave Theory and Techniques*, vol. 48, no. 4, pp. 740–743, Apr. 2000.

[10] N. Nagai, T. Imai, R. Fukasawa, K. Kato, and K. Yamauchi, "Analysis of the intermolecular interaction of nanocomposites by THz spectroscopy", *Applied Physics Letters*, vol. 85, no. 18, pp. 4010, Nov. 2004.

[11] H.-T. Chen, R. Kersting, and G. C. Cho, "Terahertz imaging with nanometer resolution", *Applied Physics Letters*, vol. 83, no. 15, pp. 3009, Oct. 2003.

[12] A. J. Fitzgerald, V. P. Wallace, M. Jimenez-Linan, L. Bobrow, R. J. Pye, A. D. Purushotham, and D. D. Arnone, "Terahertz pulsed imaging of human breast tumors.", *Radiology*, vol. 239, no. 2, pp. 533–40, May 2006.

[13] R. M. Woodward, B. E. Cole, V. P. Wallace, R. J. Pye, D. D. Arnone, E. H. Linfield, and M. Pepper, "Terahertz pulse imaging in reflection geometry of human skin cancer and skin tissue", *Physics in Medicine and Biology*, vol. 47, no. 21, pp. 3853–3863, Nov. 2002.

[14] M. Hirmer, S. N. Danilov, S. Giglberger, J. Putzger, A. Niklas, A. Jäger, K.-A. Hiller, S. Löffler, G. Schmalz, B. Redlich, I. Schulz, G. Monkman, and S. D. Ganichev, "Spectroscopic Study of Human Teeth and Blood from Visible to Terahertz Frequencies for Clinical Diagnosis of Dental Pulp Vitality", *Journal*

of Infrared, Millimeter, and Terahertz Waves, vol. 33, no. 3, pp. 366–375, Feb. 2012.

[15] D. Crawley, C. Longbottom, V. P. Wallace, B. Cole, D. Arnone, and M. Pepper, "Three-dimensional terahertz pulse imaging of dental tissue.", *Journal of biomedical optics*, vol. 8, no. 2, pp. 303–7, Apr. 2003.

[16] M. C. Kemp, "Security applications of terahertz technology", in *Proceedings of SPIE*. 2003, vol. 5070, pp. 44–52, SPIE.

[17] Y.-C. Shen, "Terahertz pulsed spectroscopy and imaging for pharmaceutical applications: a review.", *International journal of pharmaceutics*, vol. 417, no. 1-2, pp. 48–60, Sept. 2011.

[18] T. Kiwa, M. Tonouchi, M. Yamashita, and K. Kawase, "Laser terahertz-emission microscope for inspecting electrical faults in integrated circuits.", *Optics letters*, vol. 28, no. 21, pp. 2058–60, Nov. 2003.

[19] E. F. Nichols and J. D. Tear, "Joining the Infra-Red and Electric Wave Spectra", *Astrophysical Journal*, vol. 61, pp. 17, 1925.

[20] H. Eisele and G. I. Haddad, "Two-terminal millimeter-wave sources", *IEEE Transactions on Microwave Theory and Techniques*, vol. 46, no. 6, pp. 739–746, June 1998.

[21] E. R. Brown, J. R. Soderstrom, C. D. Parker, L. J. Mahoney, K. M. Molvar, and T. C. McGill, "Oscillations up to 712 GHz in InAs/AlSb resonant-tunneling diodes", *Applied Physics Letters*, vol. 58, no. 20, pp. 2291, May 1991.

[22] A. Maestrini, J. Ward, J. Gill, H. Javadi, E. Schlecht, G. Chattopadhyay, F. Maiwald, N. R. Erickson, and I. Mehdi, "A 1.7-1.9 THz local oscillator source", *IEEE Microwave and Wireless Components Letters*, vol. 14, no. 6, pp. 253–255, June 2004.

[23] O. Momeni and E. Afshari, "High Power Terahertz and Millimeter-Wave Oscillator Design: A Systematic Approach", *IEEE Journal of Solid-State Circuits*, vol. 46, no. 3, pp. 583–597, Mar. 2011.

[24] S. H. Gold and G. S. Nusinovich, "Review of high-power microwave source research", *Review of Scientific Instruments*, vol. 68, no. 11, pp. 3945, Nov. 1997.

[25] J. Tucek, D. Gallagher, K. Kreischer, and R. Mihailovich, "A compact, high power, 0.65 THz source", in *2008 IEEE International Vacuum Electronics Conference*. May 2008, pp. 16–17, IEEE.

[26] B. P. Gorshunov, A. A. Volkov, A. S. Prokhorov, and I. E. Spektor, "Methods of terahertz-subterahertz BWO spectroscopy of conducting materials", *Physics of the Solid State*, vol. 50, no. 11, pp. 2001–2012, Nov. 2008.

[27] R. Köhler, A. Tredicucci, F. Beltram, H. E. Beere, E. H. Linfield, A. G. Davies, D. A. Ritchie, R. C. Iotti, and F. Rossi, "Terahertz semiconductor-heterostructure laser.", *Nature*, vol. 417, no. 6885, pp. 156–9, May 2002.

[28] G. Scalari, C. Walther, M. Fischer, R. Terazzi, H. E. Beere, D. Ritchie, and J. Faist, "THz and sub-THz quantum cascade lasers", *Laser & Photonics Review*, vol. 3, no. 1-2, pp. 45–66, Feb. 2009.

[29] S. Fathololoumi, E. Dupont, C. W. I. Chan, Z. R. Wasilewski, S. R. Laframboise, D. Ban, A. Mátyás, C. Jirauschek, Q. Hu, and H. C. Liu, "Terahertz quantum cascade lasers operating up to 200 K with optimized oscillator strength and improved injection tunneling", *Optics Express*, vol. 20, no. 4, pp. 3866, Feb. 2012.

[30] S. Y. Tochitsky, J. E. Ralph, C. Sung, and C. Joshi, "Generation of megawatt-power terahertz pulses by noncollinear difference-frequency mixing in GaAs", *Journal of Applied Physics*, vol. 98, no. 2, pp. 026101, July 2005.

[31] G. Chang, C. J. Divin, J. Yang, M. A. Musheinish, S. L. Williamson, A. Galvanauskas, and T. B. Norris, "GaP waveguide emitters for high power broadband THz generation pumped by Yb-doped fiber lasers", *Optics Express*, vol. 15, no. 25, pp. 16308, Dec. 2007.

[32] Y. Sasaki, A. Yuri, K. Kawase, and H. Ito, "Terahertz-wave surface-emitted difference frequency generation in slant-stripe-type periodically poled LiNbO[sub 3] crystal", *Applied Physics Letters*, vol. 81, no. 18, pp. 3323, Oct. 2002.

[33] K. L. Vodopyanov, M. M. Fejer, X. Yu, J. S. Harris, Y.-S. Lee, W. C. Hurlbut, V. G. Kozlov, D. Bliss, and C. Lynch, "Terahertz-wave generation in quasi-phase-matched GaAs", *Applied Physics Letters*, vol. 89, no. 14, pp. 141119, Oct. 2006.

[34] A. G. Stepanov, J. Kuhl, I. Z. Kozma, E. Riedle, G. Almási, and J. Hebling, "Scaling up the energy of THz pulses created by optical rectification", *Optics Express*, vol. 13, no. 15, pp. 5762, July 2005.

[35] P. N. Butcher and D. Cotter, *The Elements of Nonlinear Optics*, Cambridge University Press, Cambridge, U. K., 1990.

[36] S. Preu, G. H. Dohler, S. Malzer, L. J. Wang, and A. C. Gossard, "Tunable, continuous-wave Terahertz photomixer sources and applications", *Journal of Applied Physics*, vol. 109, no. 6, pp. 061301, Mar. 2011.

[37] J. E. Bjarnason, T. L. J. Chan, A. W. M. Lee, E. R. Brown, D. C. Driscoll, M. Hanson, A. C. Gossard, and R. E. Muller, "ErAs:GaAs photomixer with two-decade tunability and 12μW peak output power", *Applied Physics Letters*, vol. 85, no. 18, pp. 3983, Nov. 2004.

[38] E. Peytavit, S. Lepilliet, F. Hindle, C. Coinon, T. Akalin, G. Ducournau, G. Mouret, and J.-F. Lampin, "Milliwatt-level output power in the sub-terahertz range generated by photomixing in a GaAs photoconductor", *Applied Physics Letters*, vol. 99, no. 22, pp. 223508, Nov. 2011.

[39] P. C. Upadhya, W. Fan, A. Burnett, J. Cunningham, A. G. Davies, E. H. Linfield, J. Lloyd-Hughes, E. Castro-Camus, M. B. Johnston, and H. E. Beere, "Excitation-density-dependent generation of broadband terahertz radiation in an asymmetrically excited photoconductive antenna", *Optics Letters*, vol. 32, no. 16, pp. 2297, Aug. 2007.

[40] H. Roehle, R. J. B. Dietz, H. J. Hensel, J. Böttcher, H. Künzel, D. Stanze, M. Schell, and B. Sartorius, "Next generation 15 m terahertz antennas: mesastructuring of InGaAs/InAlAs photoconductive layers", *Optics Express*, vol. 18, no. 3, pp. 2296, Jan. 2010.

[41] Z. D. Taylor, E. R. Brown, J. E. Bjarnason, M. P. Hanson, and A. C. Gossard, "Resonant-optical-cavity photoconductive switch with 0.5% conversion efficiency and 1.0W peak power", *Optics Letters*, vol. 31, no. 11, pp. 1729, June 2006.

[42] S.-G. Park, K. H. Jin, M. Yi, J. C. Ye, J. Ahn, and K.-H. Jeong, "Enhancement of terahertz pulse emission by optical nanoantenna", *ACS nano*, vol. 6, no. 3, pp. 2026–2031, Mar. 2012.

[43] D. H. Auston, K. P. Cheung, and P. R. Smith, "Picosecond photoconducting Hertzian dipoles", *Applied Physics Letters*, vol. 45, no. 3, pp. 284, 1984.

[44] C. W. Berry and M. Jarrahi, "Principles of Impedance Matching in Photoconductive Antennas", *Journal of Infrared, Millimeter, and Terahertz Waves*, pp. 1–8, Sept. 2012.

[45] C. W. Berry, N. Wang, M. R. Hashemi, M. Unlu, and M. Jarrahi, "Significant performance enhancement in photoconductive terahertz optoelectronics by incorporating plasmonic contact electrodes", *Nature Communications*, vol. 4, pp. 1622, 2013.

[46] C. W. Berry, M. R. Hashemi, M. Unlu, and M. Jarrahi, "Design, fabrication, and experimental characterization of plasmonic photoconductive terahertz emitters.", *Journal of Visualized Experiments*, vol. 77, pp. e50517, Jan. 2013.

[47] C. W. Berry and M. Jarrahi, "Terahertz generation using plasmonic photoconductive gratings", *New Journal of Physics*, vol. 14, no. 10, pp. 105029, Oct. 2012.

CHAPTER II

Conventional Photoconductive Terahertz Sources

Photoconduction has become one of the most commonly used techniques for generating terahertz waves, since the first demonstration in 1984 [1]. Photoconductive terahertz sources produce terahertz radiation through a merger of RF and optical techniques.

2.1 Operation

In their most basic form, photoconductive terahertz sources consist of an antenna designed for terahertz frequencies connected to a photo-absorbing semiconductor substrate. In operation an optical pump beam impinges on the photo-absorbing semiconductor, generating electron-hole pairs in the substrate. The photoconductor's contact electrodes connect to an external voltage supply which generates an electric field in the semiconductor. Under the influence of the applied electric field, the photocarriers begin to drift toward their corresponding contact electrodes. After reaching the photoconductor contact electrodes, the collected photocurrent drives a terahertz antenna connected to the contact electrodes.

To produce terahertz radiation, the photocurrent driving the terahertz antenna must carry terahertz frequency components. This can be accomplished by using an optical pump having an intensity envelope with terahertz frequency components, since the photocarrier generation rate in the semiconductor follows the intensity envelope the optical pump. Photoconductive terahertz sources can operate in two operation

modes: pulsed and continuous-wave (CW). In the pulsed mode, photoconductive terahertz sources are pumped with sub-picosecond optical pulses from a mode-locked laser to produce pulsed terahertz current and radiation. In the CW mode, photoconductive terahertz sources are pumped with two continuous-wave optical beams with a terahertz frequency difference to produce CW terahertz current and radiation at the difference frequency of the two optical beams.

The principle of operation in photoconductive terahertz sources, also referred to as photoconductive antennas, is very similar to conventional antennas. In both cases, the acceleration of charges due to a time-varying electrical current gives rise to time-varying electric and magnetic fields which will radiate from the antenna. The differences between the nature of their input signal, however, impose different design rules. While several small-signal and large-signal models have been presented for describing photoconductive antenna operation [2–5], little investigation has focused on the impedance matching requirements of photoconductive antennas in various operational settings.

Figure 2.1a shows the equivalent circuit model of a conventional antenna in transmission mode, where R_s and X_s are the resistive and reactive components of the input source, and R_A and X_A are the antenna radiation resistance and reactive components, respectively. Radiated power from the conventional antenna is given by

$$P_{rad}(\omega) = \frac{1}{2}|V_{in}(\omega)|^2 \xi \frac{R_A}{(R_A + R_s)^2 + (X_A + X_s)^2} \tag{2.1}$$

where V_{in} is the input voltage to the antenna and ξ is the antenna efficiency. As the general impedance matching rule predicts, the antenna impedance should be conjugate-matched to the source impedance ($R_A = R_s$ and $X_s = -X_a$) to maximize the radiated power [6].

The major difference of a photoconductive antenna with a conventional antenna is the optical nature of the input signal in the photoconductive antenna, which can

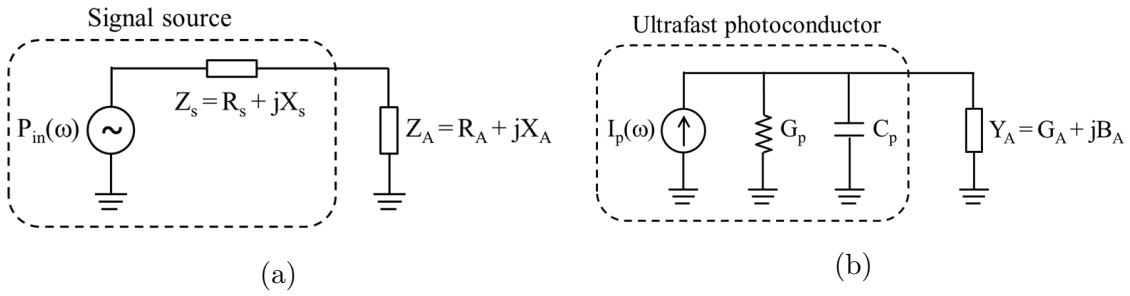

Figure 2.1: The equivalent circuit model of (a) a conventional antenna and (b) a photoconductive antenna.

be modeled as a current source. At low pump powers, the amplitude of the photoconductor current, $I(\omega)$, at the angular frequency, ω, is linearly proportional to the envelope of the optical pump power at that frequency, $P_{opt}(\omega)$. Figure 2.1b shows the equivalent circuit model of a photoconductive antenna, where G_p and C_p are the conductance and capacitance of the ultrafast photoconductor connected to a terahertz antenna represented by a complex admittance $Y_A = G_A + jB_A$ [2, 3], which includes the inductance of the photoconductor bias line. Radiated power from the photoconductive antenna is given by

$$P_{rad}(\omega) = \frac{1}{2}|S_p(\omega)P_{opt}(\omega)|^2 \xi \frac{G_A}{(G_A + G_p)^2 + (\omega C_p + B_A)^2} \tag{2.2}$$

where $S_p(\omega)$ is the photoconductor current responsivity. As it can be seen from Eq. 2.2, conjugate-matching the photoconductor impedance to the antenna impedance does not necessarily maximize the radiated power from the photoconductive antenna. Independent of the photoconductive antenna structure, in order to maximize the radiated power from the photoconductive antenna, the reactive parasitic loading to the antenna should be minimized $(G_A + G_p) \gg (\omega C_p + B_A)$. This can be achieved by maintaining low photoconductor capacitive loading and high bias line inductive loading to the antenna in broadband operational settings or by designing a bias line with a negative shunt susceptance that cancels the parasitic capacitance in narrowband operational settings [2, 3]. However, depending on the photoconductor conductance

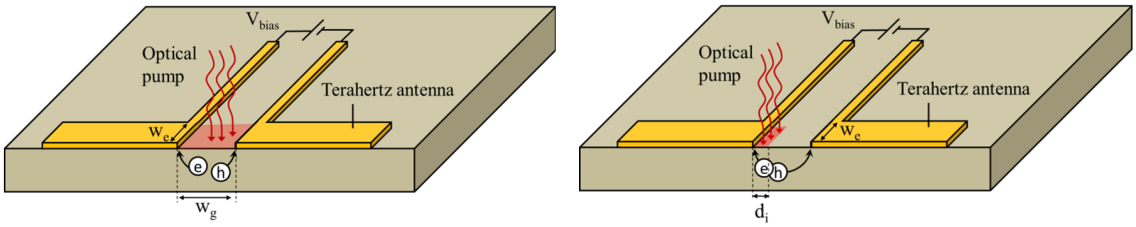

(a) (b)

Figure 2.2: Schematic diagrams of photoconductive terahertz sources. The semiconductor gap between photoconductor contact electrodes (a) uniformly illuminated by the optical pump and (b) asymmetrically illuminated by the optical pump near the anode.

dependence on optical pump power, the optimum photoconductor conductance is not necessarily determined by the well-known conjugate-matching rule and should be calculated for each photoconductive antenna structure separately. In the following sections, we analyze the impedance optimization criteria for two types of photoconductive antenna structures. The two categories are selected based on the photoconductor conductance dependence on the optical pump power.

2.1.1 Symmetrically Excited Sources

The first category of photoconductive antennas that will be analyzed consists of ultrafast photoconductors with the semiconductor gap between their contact electrodes fully illuminated by the optical pump. Figure 2.2a shows a photoconductive antenna from this category. If the pump photons have a uniform intensity across the photoconductor active area and are uniformly absorbed within the absorption depth $1/\alpha$, the density of carriers generated within the photoconductor active region can be calculated from [7–9].

$$\frac{dn}{dt} = \frac{\eta_e \alpha}{h\nu w_g w_e} P_{opt} - \frac{n}{\tau} \tag{2.3}$$

where η_e is the photoconductor external quantum efficiency (number of generated

electron-hole pairs per each incident photon), τ is the carrier lifetime in the semiconductor, hv is the photon energy, w_g is the gap between photoconductor contact electrodes, and w_e is the width of the photoconductor active region. Therefore, the photogenerated carrier density is calculated as [4]

$$n(t) = \frac{\eta_e \alpha \tau}{h\nu w_g w_e} P_{opt}(0) \Bigg[1 + \frac{P_{opt}(\omega_1) sin(\omega_1 t + \phi(\omega_1))}{P_{opt}(0)\sqrt{1+\omega_1^2\tau^2}} + \frac{P_{opt}(\omega_2) sin(\omega_2 t + \phi(\omega_2))}{P_{opt}(0)\sqrt{1+\omega_2^2\tau^2}} + \cdots \Bigg] \tag{2.4}$$

where $\phi(\omega) = tan^{-1}(1/\omega\tau)$, $P_{opt}(0)$ is the DC component of the envelope of the optical pump, and $P_{opt}(\omega_i) = \gamma(\omega_i) P_{opt}(0)$ is the frequency components of the envelope of the optical pump at angular frequency ω_i $(i = 1, 2, \dots)$. It should be noted that angular frequencies ω_i represent a single terahertz frequency for a heterodyned optical pump (for continuous-wave terahertz generation) and a continuous span of terahertz frequencies for a pulsed optical pump (for pulsed terahertz generation). Using the calculated photogenerated carrier density, the photoconductor conductance and photocurrent can be calculated as [3, 4]

$$G_p = \frac{\eta_e q \tau (\mu_e + \mu_h)}{h\nu w_g^2} P_{opt}(0) \Bigg[1 + \frac{\gamma(\omega_1) sin(\omega_1 t + \phi(\omega_1))}{\sqrt{1+\omega_1^2\tau^2}} + \frac{\gamma(\omega_2) sin(\omega_2 t + \phi(\omega_2))}{\sqrt{1+\omega_2^2\tau^2}} + \cdots \Bigg] \tag{2.5}$$

$$I_p = \frac{\eta_e q \tau (v_e + v_h)}{h\nu w_g} P_{opt}(0) \Bigg[1 + \frac{\gamma(\omega_1) sin(\omega_1 t + \phi(\omega_1))}{\sqrt{1+\omega_1^2\tau^2}} + \frac{\gamma(\omega_2) sin(\omega_2 t + \phi(\omega_2))}{\sqrt{1+\omega_2^2\tau^2}} + \cdots \Bigg] \tag{2.6}$$

where q is the electron charge, μ_e and μ_h are electron and hole mobilities, and v_e and v_g are electron and hole velocities, respectively. As it can be seen from Eq.

2.5 and 2.6, when the semiconductor gap between photoconductor contact electrodes is uniformly illuminated by the optical pump, all frequency components of the induced photocurrent $I_p(\omega)$, are linearly proportional to the average photoconductor conductance, $\overline{G_p}$

$$I_p(\omega) = \frac{v_e + v_h}{\mu_e + \mu_h} \frac{w_g \gamma(\omega)}{\sqrt{1 + \omega^2 \tau^2}} \overline{G_p} \tag{2.7}$$

Assuming a negligible reactive parasitic loading to the antenna $(G_A + \overline{G_p}) \gg (\omega C_p + B_A)$, the radiated power from the photoconductive antenna is calculated as

$$\begin{aligned} P_{rad}(\omega) &= \frac{1}{2} w_g^2 \left[\frac{v_e + v_h}{\mu_e + \mu_h} \right]^2 \frac{\gamma(\omega)^2}{1 + \omega^2 \tau^2} \xi G_A \left[\frac{\overline{G_p}}{G_A + \overline{G_p}} \right] \\ &\cong \frac{1}{2} V_{bias}^2 \frac{\gamma(\omega)^2}{1 + \omega^2 \tau^2} G_A \left[\frac{\overline{G_p}}{G_A + \overline{G_p}} \right] \end{aligned} \tag{2.8}$$

Equation 2.8 shows that the optimum photoconductor conductance that maximizes the radiated power from the photoconductive antenna is $\overline{G_p} = G_A$. Therefore, when the semiconductor gap between photoconductor contact electrodes is uniformly illuminated by the optical pump, conjugate-matching the photoconductor impedance to the antenna impedance maximizes the radiated power from the photoconductive antenna. Equation 2.8 also shows the direct dependence of the radiated power on the antenna radiation resistance at a given optical pump power level. Therefore, the use of high radiation resistance antennas [10–12] is as important as the impedance matching criteria in achieving high optical-to-terahertz conversion efficiencies. Without loss of generality, the discussed analysis is equally applicable for calculating the optimum design parameters in photoconductive antennas with interdigitated electrodes.

2.1.2 Asymmetrically Excited Sources

The second category of photoconductive antennas that will be analyzed consists of ultrafast photoconductors with the semiconductor gap between their contact electrodes partially illuminated by the optical pump. Figure 2.2b shows a photoconductive antenna from this category with an asymmetric pump illumination near the photoconductor anode contact. This design is attractive due to the nonlinear bias field increase near the anode contact, providing a strong acceleration field for electons and enabling optical-to-terahertz conversion efficiency enhancement [13]. Similar analysis can be used to calculate the induced photocurrent. If the pump photons have a uniform intensity within a distance d_i from anode contact and uniformly absorbed within the absorption depth $1/\alpha$, the frequency components of the induced photocurrent $I_p(\omega)$ are calculated as

$$I_p(\omega) = \frac{\eta_e q \tau (v_e + v_h)}{h\nu d_i} P_{opt}(0) \frac{\gamma(\omega)}{\sqrt{1+\omega^2\tau^2}} \tag{2.9}$$

Since the semiconductor gap between photoconductor contact electrodes is partially illuminated, photoconductor conductance is not linearly proportional to the optical pump power and is calculated as

$$G_p = \frac{1}{\dfrac{h\nu d_i^2}{\eta_e q \tau (\mu_e + \mu_h) P_{opt}(0)} + \dfrac{1}{G_{p-dark}}} \tag{2.10}$$

where G_{p-dark} is the conductance of the un-illuminated semiconductor area between photoconductor contact electrodes. Assuming negligible reactive parasitic loading to the antenna, the radiated power from discussed photoconductive antenna is calculated as

$$P_{rad}(\omega) = \frac{1}{2}\left[\frac{\eta_e q\tau(v_e + v_h)}{h\nu d_i}\right]^2 \frac{\gamma(\omega)^2}{1+\omega^2\tau^2} P_{opt}^2(0)\xi \frac{G_A}{(G_A+G_p)^2} \tag{2.11}$$

In order to design a photoconductive antenna with optimum optical-to-terahertz conversion efficiency, the radiated power (Eq. 2.11) as a function of photoconductor conductance (Eq. 2.10) should be calculated and maximized by appropriate choice of photoconductor geometry and operational settings. For very small illumination spot sizes ($d_i \ll w_g$) and short-carrier photo-absorbing substrates, the photoconductor conductance would be the same as the photoconductor dark conductance (independent of pump power level). Therefore, the optimum photoconductor conductance that maximizes the radiated power from the photoconductive antenna is $G_p \ll G_A$, different from the well-known impedance conjugate-matching criteria. Moreover, similar to the photoconductive antennas with the semiconductor gap between contact electrodes fully illuminated by the optical pump, the use of high radiation resistance antennas [10–12] is crucial for achieving high optical-to-terahertz conversion efficiencies.

Equation 2.11 shows that at the same optical pump power level, an asymmetrically pumped photoconductive antenna near anode contact electrode (Fig. 2.2b) can offer more than four times higher radiated power compared with an identical photoconductive antenna with the semiconductor gap between contact electrodes fully illuminated by the optical pump (Fig. 2.2a). This is possible because of the design flexibility of asymmetrically pumped photoconductive antennas that allows optimizing the photoconductor's conductance independent of the pump power level. Moreover, the use of low-conductance photoconductors, which is required for high optical-to-terahertz conversion efficiencies, offers an additional advantage of low DC power consumption by maintaining low DC currents even at high pump power levels.

Tight focusing of the optical pump can significantly enhance the radiated power of asymmetrically pumped photoconductive antennas at low pump power levels by reducing the carrier transport path to the anode electrode, but at high optical pump

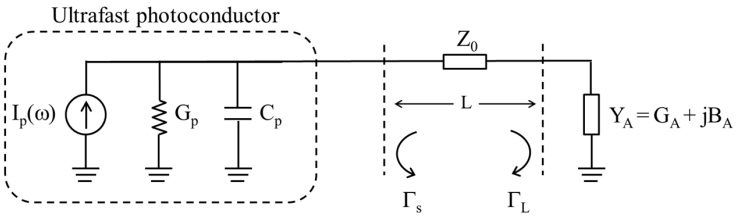

Figure 2.3: The equivalent circuit model of a photoconductive emitter with a transmission line connecting the ultrafast photoconductor to the terahertz radiating antenna.

power levels, several saturation mechanisms reduce the optical-to-terahertz conversion efficiency of photoconductive antennas. One such mechanism, the carrier screening effect, arises from the spatial separation of photocarriers in the substrate. The charge separation generates an electric field opposing and screening the original bias electric field. This reduces the velocity of photocarriers in the substrate, and hence the current feeding the antenna, and becomes important at high carrier densities [8, 14]. Additionally, optical absorption in the substrate decreases at higher optical intensities due to the filling of the finite number of states in the semiconductor band structure through an effect known as absorption bleaching. Finally, at high current densities, joule heating in the semiconductor will lead to device failure through thermal breakdown [15]. As will be shown in Chapter III, utilizing nanoscale contact electrodes [16–21] in asymmetrically pumped photoconductive antennas enables suppressing the carrier screening effect, absorption bleaching, and thermal breakdown to achieve high optical-to-terahertz conversion efficiencies at high pump power levels.

It should be mentioned that the discussed photoconductor impedance optimization criteria is accurate when the ultrafast photoconductor is directly connected to the terahertz radiating antenna with a negligible connection length compared with the terahertz wavelength. When the connection length becomes comparable with the radiation wavelength [2], the corresponding transmission line should be included in the photoconductive antenna circuit model and accounted for while calculating the photoconductor's impedance optimization criteria. Figure 2.3 shows the equivalent

circuit model of a photoconductive antenna with a transmission line connecting the ultrafast photoconductor to the terahertz radiating antenna. Radiated power from the discussed photoconductive antenna is calculated as

$$P_{rad}(\omega) = \frac{1}{2}|S_p(\omega)P_{opt}(\omega)|^2 \left| \frac{1}{1-\Gamma_L\Gamma_s e^{-j2\beta L}} \right|^2 \xi \times \frac{G_A}{(Real[\frac{1}{Z_0}] + G_p)^2 + (\omega C_p + Imag[\frac{1}{Z_0}])^2} \tag{2.12}$$

where Z_0, β, and L are the characteristic impedance, wave propagation constant, and length of the transmission line, respectively, and Γ_s and Γ_L are the reflection coefficients at the photoconductor and antenna terminations of the transmission line, respectively. In case of perfect matching between the transmission line characteristic impedance and the antenna impedance, Eq. 2.12 would be the same as Eq. 2.8 and Eq. 2.11 when the semiconductor gap between photoconductor contact electrodes are fully and partially illuminated by the optical pump, respectively. Therefore, the impedance optimization criteria would be the same as the situation where the ultrafast photoconductor is directly connected to the terahertz radiating antenna with a negligible connection length compared with the terahertz wavelength. In case of a mismatch between the transmission line characteristic impedance and the antenna impedance, the terahertz signal can bounce back and forth between the photoconductor and antenna until it attenuates along the connecting transmission line. Therefore, in order to optimize the photoconductive antenna design for high power efficiency, the radiated power (Eq. 2.12) as a function of photoconductor conductance should be calculated and maximized by the appropriate choice of photoconductor parameters and operational settings.

In conclusion, using the equivalent circuit model of photoconductive antennas the optimum photoconductor impedance is calculated that maximizes the optical-to-

terahertz conversion efficiency. The analysis shows that the optimum photoconductor impedance is not necessarily determined by the well-known conjugate-matching rule and should be calculated for each photoconductive antenna structure and operational settings. When the semiconductor gap between photoconductor contact electrodes is uniformly illuminated by the optical pump, conjugate-matching the photoconductor impedance to the antenna impedance maximizes the radiated power from the photoconductive antenna. In contrast, when the semiconductor gap between photoconductor contact electrodes is partially illuminated by the optical pump near the anode, using photoconductors with resistance values much larger than the antenna radiation resistance maximizes the radiated power from the photoconductive antenna. Independent of the photoconductive antenna structure, the maximum radiated power from a photoconductive antenna is achieved when maximizing the antenna radiation resistance, while maintaining low reactive parasitic loading to the antenna. Finally, it should be mentioned that photoconductive antennas are reciprocal devices, and the described impedance optimization principles are applicable to both photoconductive terahertz sources and photoconductive terahertz detectors.

2.2 Advantages and Limitations of Photoconductive Terahertz Sources

Technological breakthroughs in the field of solid-state and fiber lasers make photoconductive emitters very promising, enabling extreme frequency tunability, high spectral purity (required for CW terahertz generation), and broad bandwidth (required for pulsed terahertz generation) while operating at room temperature. Specifically, the availability of high power (>10 W average), narrow line-width (kHz range), and wavelength tunable (10s of nm) fiber amplifiers at 1550 nm (EDFA) and 1030 nm (YDFA) wavelengths makes photoconductive terahertz emitters pumped at these pump wave-

lengths very promising for future low-cost, compact, and high-performance terahertz systems. A major advantage of photoconductive terahertz emitters over terahertz sources based on pure nonlinear optical effects is that their optical-to-terahertz conversion efficiency is not restricted by the Manley-Rowe relations, which set the upper limit for the conversion efficiency of standard nonlinear conversion processes equal to the ratio of the frequencies of the radiation involved. For instance, in terahertz generation through the nonlinear optical process of difference-frequency generation, two optical beams having a frequency difference in the terahertz range are combined in a material with a nonlinear susceptance to produce a terahertz wave. Since the creation of a single terahertz photon requires the conversion of the two optical photons, energy conservation restraints set an upper limit of the conversion efficiency equal to the ratio of the terahertz frequency to the optical frequency. In contrast, photoconductive terahertz antennas utilize additional, external energy supplied by a DC voltage supply to accelerate carriers in the substrate [22]. Each photon absorbed in a photoconductor can generate one electron-hole pair, which can radiate several terahertz photons upon reaching the terahertz antenna. In other words, the power efficiency of photoconductive sources can approach 100%, orders of magnitude higher than the Manley-Rowe limit. Despite this conversion efficiency upper limit, the low quantum-efficiency of conventional ultrafast photoconductors imposes substantially lower optical-to-terahertz conversion efficiencies in conventional photoconductive terahertz sources.

The quantum efficiency of conventional photoconductive terahertz sources is limited by the efficient collection of the generated photocarriers. Since the minimum focal size of the optical pump is limited by diffraction, conventional photoconductive terahertz sources use micrometer-scale spacing between photoconductor's contact electrodes to allow the transmission of light to the semiconductor. To efficiently produce terahertz radiation, however, the transport time the photocarriers take to reach

the photoconductor's contact electrodes should be a fraction of the oscillation period of the desired radiation [23]. The remaining carriers only contribute to the photoconductor's DC current, which can heat the device through ohmic losses and reduce bias field across the photoconductor active region through the carrier screening effect, decreasing the photocarriers' acceleration toward the contact electrodes. Therefore, the majority of photoconductive terahertz emitters use short-carrier lifetime semiconductors to suppress the excess DC current by forcing the charge carriers with long transport times to the contact electrodes to recombine before reaching the contact electrodes. As an example, conventional photoconductive terahertz emitters based on short-carrier lifetime GaAs pumped at 800 nm use contact electrodes spacing of $\sim$2 µm to operate within the diffraction limit [24]. Considering the maximum carrier drift velocity of $\sim 10^7$ cm/s in GaAs, only $\sim$5% of the photocarriers can reach the photoconductor contact electrodes within a picosecond, and the majority of the carriers recombine inside the short-carrier lifetime substrate. Additionally, the quantum efficiency of photoconductive terahertz emitters is further degraded at high pump power levels due to the carrier screening effect and thermal breakdown. Large-aperture photoconductive antennas and a variety of electrode configurations have been employed to suppress such effects and enhance the carrier accelerating field strength [25–32].

The use of short-carrier lifetime semiconductors for conventional diffraction-limited photoconductive terahertz emitters introduces a number of shortcomings that lead to further power efficiency degradation. The most commonly used short-carrier lifetime substrates for operation at $\sim$800 nm pump wavelengths are prepared by growing GaAs at low temperatures ($\sim$200 °C) [33, 34] or introducing ErAs islands while growing GaAs [35, 36]. At 1550 nm and 1030 nm wavelengths where high power, tunable, narrow line-width and compact lasers are commercially available, short-carrier lifetime substrates are prepared by growing InGaAs at low temperatures [37], ion irradiation of InGaAs [38–40], or introducing ErAs islands while growing InGaAs [41, 42]. An

alternative scheme is based on embedding low-temperature grown InGaAs between InAlAs layers to offer high photoconductor dark resistivity levels [43]. All of the listed techniques for developing short-carrier lifetime substrates incorporate a high density of trap sites within the semiconductor lattice and therefore degrade carrier mobility and photoconductor quantum efficiency, significantly. The high density of trap sites in short-carrier lifetime semiconductors also degrades semiconductor's thermal conductivity [15], which leads to a premature thermal breakdown of photoconductors at high optical pump power levels.

References

[1] D. H. Auston, K. P. Cheung, and P. R. Smith, "Picosecond photoconducting Hertzian dipoles", *Applied Physics Letters*, vol. 45, no. 3, pp. 284, 1984.

[2] S. M. Duffy, S. Verghese, A. McIntosh, A. Jackson, A. C. Gossard, and S. Matsuura, "Accurate modeling of dual dipole and slot elements used with photomixers for coherent terahertz output power", *IEEE Transactions on Microwave Theory and Techniques*, vol. 49, no. 6, pp. 1032–1038, June 2001.

[3] E. R. Brown, "THz generation by photomixing in ultrafast photoconductors", *International journal of high speed electronics and systems*, vol. 13, no. 2, pp. 497–546, June 2003.

[4] E. R. Brown, F. W. Smith, and K. A. McIntosh, "Coherent millimeter-wave generation by heterodyne conversion in low-temperature-grown GaAs photoconductors", *Journal of Applied Physics*, vol. 73, no. 3, pp. 1480–1484, Feb. 1993.

[5] I. S. Gregory, C. Baker, W. R. Tribe, I. V. Bradley, M. J. Evans, E. H. Linfield, A. G. Davies, and M. Missous, "Optimization of photomixers and antennas for continuous-wave terahertz emission", *IEEE Journal of Quantum Electronics*, vol. 41, no. 5, pp. 717–728, May 2005.

[6] F. T. Ulaby, *Fundamentals of Applied Electromagnetics*, Prentice Hall, Upper Saddle River, New Jersey, 1997.

[7] P. U. Jepsen, R. H. Jacobsen, and S. R. Keiding, "Generation and detection of terahertz pulses from biased semiconductor antennas", *Journal of the Optical Society of America B*, vol. 13, no. 11, pp. 2424, Nov. 1996.

[8] Z. Piao, M. Tani, and K. Sakai, "Carrier Dynamics and Terahertz Radiation in Photoconductive Antennas", *Japanese Journal of Applied Physics*, vol. 39, no. Part 1, No. 1, pp. 96–100, Jan. 2000.

[9] K. Ezdi, B. Heinen, C. Jördens, N. Vieweg, N. Krumbholz, R. Wilk, M. Mikulics, and M. Koch, "A hybrid time-domain model for pulsed terahertz dipole antennas", *Journal of the European Optical Society - Rapid Publications*, vol. 4, pp. 09001, 2009.

[10] E. R. Brown, A. W. M. Lee, B. S. Navi, and J. E. Bjarnason, "Characterization of a planar self-complementary square-spiral antenna in the THz region", *Microwave and Optical Technology Letters*, vol. 48, no. 3, pp. 524–529, Mar. 2006.

[11] Y. Huo, G. W. Taylor, and R. Bansal, "Planar Log-Periodic Antennas on Extended Hemishperical Silicon Lenses for Millimeter/Submillimeter Wave Detection Applications", *International Journal of Infrared and Millimeter Waves*, vol. 23, no. 6, pp. 819–839, 2002.

[12] K. Ezdi, M. N. Islam, Y. A. N. Reddy, C. Jördens, A. Enders, and M. Koch, "A numerical study of photoconductive dipole antennas: the real emission frequency and an improved antenna design", in *Millimeter-Wave and Terahertz Photonics*, Strasbourg, France, Apr. 2006, p. 61940G.

[13] S. E. Ralph and D. R. Grischkowsky, "Trap-enhanced electric fields in semi-insulators: The role of electrical and optical carrier injection", *Applied Physics Letters*, vol. 59, no. 16, pp. 1972, Oct. 1991.

[14] G. C. Loata, M. D. Thomson, T. Loffler, and H. G. Roskos, "Radiation field screening in photoconductive antennae studied via pulsed terahertz emission spectroscopy", *Applied Physics Letters*, vol. 91, no. 23, pp. 232506, Dec. 2007.

[15] A. W. Jackson, J. P. Ibbetson, A. C. Gossard, and U. K. Mishra, "Reduced thermal conductivity in low-temperature-grown GaAs", *Applied Physics Letters*, vol. 74, no. 16, pp. 2325, Apr. 1999.

[16] C. W. Berry and M. Jarrahi, "Terahertz generation using plasmonic photoconductive gratings", *New Journal of Physics*, vol. 14, no. 10, pp. 105029, Oct. 2012.

[17] B.-Y. Hsieh and M. Jarrahi, "Analysis of periodic metallic nano-slits for efficient interaction of terahertz and optical waves at nano-scale dimensions", *Journal of Applied Physics*, vol. 109, no. 8, pp. 084326, Apr. 2011.

[18] B.-Y. Hsieh, N. Wang, and M. Jarrahi, "Toward Ultrafast Pump-Probe Measurements at the Nanoscale", *Optics and Photonics News*, vol. 22, no. 12, pp. 48, Dec. 2011.

[19] C. W. Berry and M. Jarrahi, "Plasmonically-Enhanced Localization of Light into Photoconductive Antennas - OSA Technical Digest (CD)", in *Conference on Lasers and Electro-Optics*. May 2010, p. CFI2, Optical Society of America.

[20] C. W. Berry and M. Jarrahi, "Ultrafast photoconductors based on plasmonic gratings", in *2011 International Conference on Infrared, Millimeter, and Terahertz Waves*. Oct. 2011, pp. 1–2, IEEE.

[21] C. W. Berry and M. Jarrahi, "Plasmonic Photoconductive Terahertz Emitters Based on Nanoscale Gratings - OSA Technical Digest (online)", in *CLEO: Science and Innovations*. May 2012, p. CF2M.1, Optical Society of America.

[22] J. B. Khurgin, "Comparison of different optical methods of THz generation", in *Proc. SPIE 3624, Ultrafast Phenomena in Semiconductors III*, K.-T. F. Tsen, Ed. May 1999, pp. 128–139, International Society for Optics and Photonics.

[23] S. Preu, G. H. Dohler, S. Malzer, L. J. Wang, and A. C. Gossard, "Tunable, continuous-wave Terahertz photomixer sources and applications", *Journal of Applied Physics*, vol. 109, no. 6, pp. 061301, Mar. 2011.

[24] J. E. Bjarnason, T. L. J. Chan, A. W. M. Lee, E. R. Brown, D. C. Driscoll, M. Hanson, A. C. Gossard, and R. E. Muller, "ErAs:GaAs photomixer with two-decade tunability and 12μW peak output power", *Applied Physics Letters*, vol. 85, no. 18, pp. 3983, Nov. 2004.

[25] M. Awad, M. Nagel, H. Kurz, J. Herfort, and K. Ploog, "Characterization of low temperature GaAs antenna array terahertz emitters", *Applied Physics Letters*, vol. 91, no. 18, pp. 181124, Nov. 2007.

[26] M. Beck, H. Schäfer, G. Klatt, J. Demsar, S. Winnerl, M. Helm, and T. Dekorsy, "Impulsive terahertz radiation with high electric fields from an amplifier-driven large-area photoconductive antenna", *Optics Express*, vol. 18, no. 9, pp. 9251, Apr. 2010.

[27] M. Jarrahi and T. H. Lee, "High-power tunable terahertz generation based on photoconductive antenna arrays", in *2008 IEEE MTT-S International Microwave Symposium Digest*. June 2008, pp. 391–394, IEEE.

[28] M. Jarrahi, "Terahertz Radiation-Band Engineering Through Spatial Beam-Shaping", *IEEE Photonics Technology Letters*, vol. 21, no. 13, pp. 830–832, July 2009.

[29] T. Hattori, K. Egawa, S.-i. Ookuma, and T. Itatani, "Intense Terahertz Pulses from Large-Aperture Antenna with Interdigitated Electrodes", *Japanese Journal of Applied Physics*, vol. 45, no. No. 15, pp. L422–L424, Apr. 2006.

[30] J. H. Kim, A. Polley, and S. E. Ralph, "Efficient photoconductive terahertz source using line excitation", *Optics Letters*, vol. 30, no. 18, pp. 2490, Sept. 2005.

[31] H. Roehle, R. J. B. Dietz, H. J. Hensel, J. Böttcher, H. Künzel, D. Stanze, M. Schell, and B. Sartorius, "Next generation 15 m terahertz antennas: mesa-structuring of InGaAs/InAlAs photoconductive layers", *Optics Express*, vol. 18, no. 3, pp. 2296, Jan. 2010.

[32] Z. D. Taylor, E. R. Brown, J. E. Bjarnason, M. P. Hanson, and A. C. Gossard, "Resonant-optical-cavity photoconductive switch with 0.5% conversion efficiency and 1.0W peak power", *Optics Letters*, vol. 31, no. 11, pp. 1729, June 2006.

[33] A. C. Warren, N. Katzenellenbogen, D. R. Grischkowsky, J. M. Woodall, M. R. Melloch, and N. Otsuka, "Subpicosecond, freely propagating electromagnetic pulse generation and detection using GaAs:As epilayers", *Applied Physics Letters*, vol. 58, no. 14, pp. 1512, Apr. 1991.

[34] Y. C. Shen, P. C. Upadhya, H. E. Beere, E. H. Linfield, A. G. Davies, I. S. Gregory, C. Baker, W. R. Tribe, and M. J. Evans, "Generation and detection of ultrabroadband terahertz radiation using photoconductive emitters and receivers", *Applied Physics Letters*, vol. 85, no. 2, pp. 164, July 2004.

[35] C. Kadow, S. B. Fleischer, J. P. Ibbetson, J. E. Bowers, A. C. Gossard, J. W. Dong, and C. J. Palmstrø m, "Self-assembled ErAs islands in GaAs: Growth and subpicosecond carrier dynamics", *Applied Physics Letters*, vol. 75, no. 22, pp. 3548, Nov. 1999.

[36] M. Griebel, J. H. Smet, D. C. Driscoll, J. Kuhl, C. A. Diez, N. Freytag, C. Kadow, A. C. Gossard, and K. Von Klitzing, "Tunable subpicosecond optoelectronic transduction in superlattices of self-assembled ErAs nanoislands.", *Nature materials*, vol. 2, no. 2, pp. 122–6, Feb. 2003.

[37] R. Takahashi, Y. Kawamura, T. Kagawa, and H. Iwamura, "Ultrafast 1.55-μm photoresponses in low-temperature-grown InGaAs/InAlAs quantum wells", *Applied Physics Letters*, vol. 65, no. 14, pp. 1790, Oct. 1994.

[38] J. Mangeney, N. Chimot, L. Meignien, N. Zerounian, P. Crozat, K. Blary, J. F. Lampin, and P. Mounaix, "Emission characteristics of ion-irradiated In_0.53Ga_0.47As based photoconductive antennas excited at 1.55 m", *Optics Express*, vol. 15, no. 14, pp. 8943, July 2007.

[39] C. Carmody, H. H. Tan, C. Jagadish, A. Gaarder, and S. Marcinkevicius, "Ion-implanted In[sub 0.53]Ga[sub 0.47]As for ultrafast optoelectronic applications", *Applied Physics Letters*, vol. 82, no. 22, pp. 3913, June 2003.

[40] M. Suzuki and M. Tonouchi, "Fe-implanted InGaAs terahertz emitters for 1.56μm wavelength excitation", *Applied Physics Letters*, vol. 86, no. 5, pp. 051104, Jan. 2005.

[41] D. C. Driscoll, M. P. Hanson, A. C. Gossard, and E. R. Brown, "Ultrafast photoresponse at 1.55 μm in InGaAs with embedded semimetallic ErAs nanoparticles", *Applied Physics Letters*, vol. 86, pp. 051908, 2005.

[42] F. Ospald, D. Maryenko, K. von Klitzing, D. C. Driscoll, M. P. Hanson, H. Lu, A. C. Gossard, and J. H. Smet, "1.55 μm ultrafast photoconductive switches based on ErAs:InGaAs", *Applied Physics Letters*, vol. 92, no. 13, pp. 131117, Apr. 2008.

[43] B. Sartorius, H. Roehle, H. Künzel, J. Böttcher, M. Schlak, D. Stanze, H. Venghaus, and M. Schell, "All-fiber terahertz time-domain spectrometer operating at 1.5 μm telecom wavelengths", *Optics Express*, vol. 16, no. 13, pp. 9565, June 2008.

CHAPTER III

Plasmonic Electrode Based Photoconductive Terahertz Sources

3.1 Overview

The efficiency of photoconductive terahertz sources is determined by their ability to convert the terahertz-modulated optical input into a terahertz electrical current feeding the antenna. Conventional designs utilize electrode spacings which are $\sim$2 µm or larger. The optical beam is focused between the electrode contacts and the generated photocarriers drift in the substrate at saturation velocity to reach the metallic contacts, as seen in Fig. 3.1a. Since the saturation velocity of carriers in GaAs, and similar materials, is $\sim 10^7$ cm/s, it would take >20 ps to collect all the generated carriers. Since this timescale is large compared to the oscillation period at 1 THz (1 ps), the electrical current does not efficiently feed the antenna. Only the photocarriers generated within approximately 100 nm of the edge of a contact electrode can start feeding the antenna within a 1 ps timescale.

To improve the optical-to-terahertz conversion efficiency, we utilize plasmonic contact electrodes to increase the current feeding the antenna on a sub-picosecond timescale, as seen in Fig. 3.1b. In operation, the optical beam is focused directly on the plasmonic structure, which is designed to efficiently transmit the optical beam into the substrate below. This allows the photocarriers to be generated almost directly below the plasmonic structure, reducing the distance the carriers have to travel

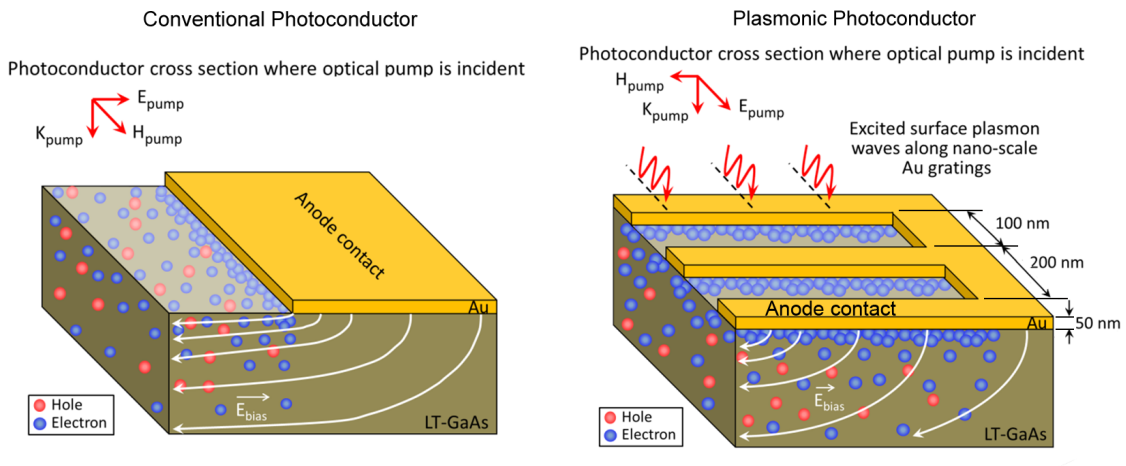

(a) (b)

Figure 3.1: Schematic of conventional and plasmonic photoconductors. The incident optical pump generates electron-hole pairs in the substrate. Electron-hole pairs are separated under an applied bias electric field and drifted toward anode and cathode contact electrodes, respectively. Upon reaching the contact electrodes, the photocurrent drives the terahertz antenna to produce radiation. (a) A conventional photoconductor. (b) A plasmonic photoconductor incorporating plasmonic contact electrodes to reduce carrier transport times to contact electrodes and, thus, increase the collected photocurrent driving the terahertz antenna.

and increasing the number of carriers which can feed the antenna in a sub-picosecond timescale.

3.1.1 Optical Transmission of Periodic Metallic Structures

The optical transmission through periodic, metallic structures has recently been the subject of much investigation [1–4]. I will limit the discussion here to the transmission of periodic, metallic slit structures illuminated by an optical beam having a magnetic field parallel to the metal lines (TM polarization), as is the case for the structures presented in this dissertation. The optical transmission through a metallic grating depends mainly on the periodicity of the grating compared to the incident wavelength. For a free standing metallic grating, there are three regimes to consider.

Wavelength $\ll$ grating period and open aperture Optical transmission can be approximated by geometrical optics. The transmission can be approximated as

the percent of open aperture of the structure.

Wavelength $\gg$ grating period Optical transmission is broadband and large. This is due to the spaces between the metallic lines preventing the acceleration of electrons in the metal. In this case, the metallic structure can be almost transparent to an incident beam with the correct polarization.

Wavelength $\sim$ grating period Optical transmission varies greatly based on the exact geometrical properties of the metallic structure, the angle of incidence, the metal permittivity, and the dielectric permittivity. For the correct momentum matching conditions, the grating can impart a horizontal momentum to the incident beam, giving rise to surface plasmon resonances which can induce or suppress optical transmission [5–7]. Additionally if the height of the metal grating is comparable to the wavelength of light, Fabry-Perot resonances can induce or suppress optical transmission [8, 9]. The remaining discussion will consider this case.

The magnitude of the wave vector for a surface plasmon on a metal-dielectric interface is given by

$$k_{SP} = \frac{\omega}{c}\sqrt{\frac{\epsilon_m \epsilon_d}{\epsilon_m + \epsilon_d}} \tag{3.1}$$

where ω is the angular frequency, c is the speed of light in vacuum, ϵ_m is the metal permittivity, and ϵ_d is the dielectric permittivity [5]. Since the magnitude of the wave vector is below the light line, excitation of a surface plasmon requires added momentum from the grating, as shown in Fig. 3.2. This can be expressed as

$$k_{SP} = k_0 sin(\theta) + G \tag{3.2}$$

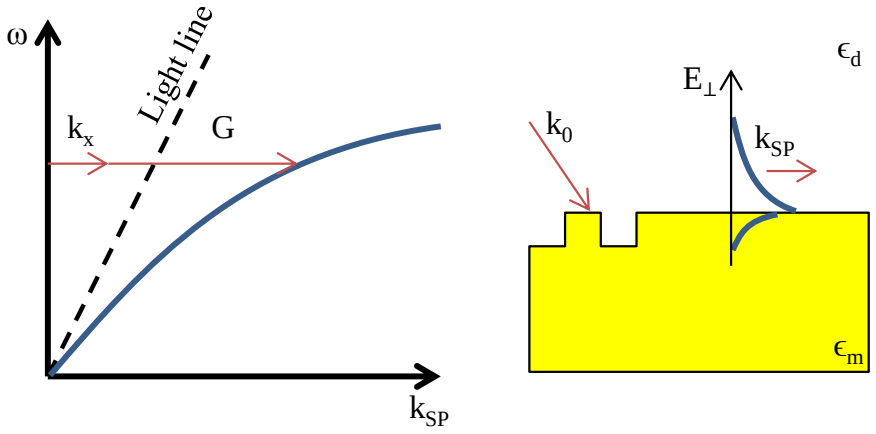

(a) (b)

Figure 3.2: Surface plasmon characteristics. (a) Surface plasmon dispersion diagram. Excitation of a surface plasmon from free space requires additional momentum, G. (b) Surface plasmon electric field profile. The electric field of a surface plasmon extends perpendicularly into the dielectric and metal, decaying exponentially. In the dielectric region, the electric field decay is on order of the wavelength. In the metal region, it is on order of the skin depth.

$$k_{SP} = k_0 sin(\theta) + m\frac{2\pi}{P} \tag{3.3}$$

where k_0 is the magnitude of the free space wave vector, θ is the angle of incidence relative to normal, $G = m\frac{2\pi}{P}$ is the added momentum from the grating, m is the diffraction order ($m = 0, \pm1, \pm2, \ldots$), and P is the grating pitch [5]. Equating Eq. 3.1 and Eq. 3.3 determines the momentum matching condition for excitation of a surface plasmon along the metal-dielectric interface. The optical transmission is normally suppressed directly at the surface plasmon resonance. At frequencies slightly detuned from the resonance, however, the optical transmission can be large and depends on the coupling strength of the various diffraction orders and surface plasmon modes [8].

When the metallic grating is placed on a substrate (e.g. a metallic grating on GaAs), the surface plasmon momentum matching considerations above and below the grating will differ [8–10]. In this case, the surface plasmon resonance from either side can facilitate or hinder optical transmission. Equating and plotting Eq. 3.1 and

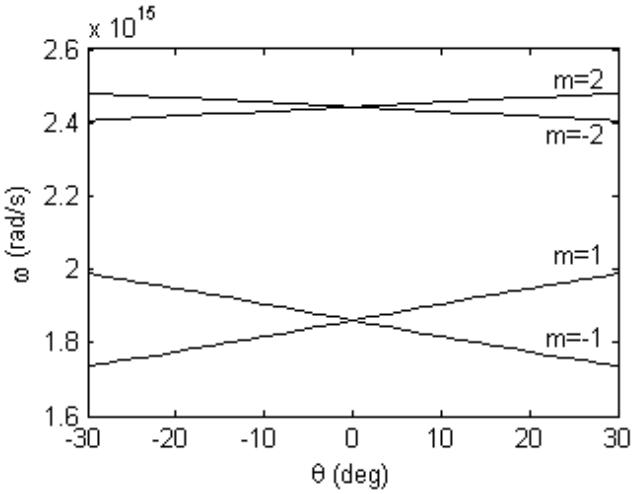

Figure 3.3: Surface plasmon dispersion diagram for the metal-substrate surface of a Au grating with 225 nm pitch on GaAs.

Eq. 3.3 as a function of frequency and angle of incidence, θ, can produce a dispersion diagram for the surface plasmon resonances. Figure 3.3 shows the dispersion diagram for a representative, Au grating with periodicity = 225 nm on a GaAs substrate at the metal-GaAs interface for various diffraction mode orders. The structures presented in this document utilize the red-shifted transmission peak associated with the $m = \pm 2$ mode.

3.2 Enhancement of Radiation Efficiency and Power

To address the power efficiency limitation of conventional photoconductive terahertz sources, we have proposed a novel photoconductive terahertz source concept which incorporates a plasmonic contact electrode configuration to offer high quantum-efficiency and ultrafast operation simultaneously, as shown in Fig. 3.4b. By using nanoscale plasmonic contact electrodes, we significantly reduce the average photogenerated carrier transport path to the photoconductor contact electrodes and increase the collected photocurrent, compared to conventional photoconductors. It should be noted that the optical-to-terahertz conversion efficiency has a quadratic relation with photoconductor quantum efficiency. By incorporating plasmonic contact electrodes,

we experimentally demonstrate enhancing the optical-to-terahertz power conversion efficiency of a conventional photoconductive terahertz emitter by up to a factor of 50.

3.2.1 Design

To demonstrate the potential of plasmonic electrodes for terahertz power enhancement, we fabricate a proof-of-concept photoconductive emitter and characterize the performance enhancement from integrating plasmonic gratings into the photoconductor's contact electrodes. It should be noted that the nanoscale plasmonic gratings could be integrated with most of the commonly used terahertz antennas. Therefore, the choice of terahertz antenna is somewhat arbitrary. In this demonstration we utilize the commonly used bowtie antenna.

Figure 3.4a shows the schematic diagram and operation concept of the implemented photoconductive emitter in the absence of plasmonic gratings (conventional scheme). The photoconductive emitter consists of an ultrafast photoconductor with 20 µm gap between anode and cathode contacts, connected to a 60 µm long bowtie antenna with maximum and minimum widths of 100 µm and 30 µm, respectively. Low-temperature-grown GaAs (LT-GaAs) is used for the photo-absorbing substrate to achieve an ultrafast photoconductor response. When a sub-picosecond optical pump at ∼800 nm wavelength range is incident on the ultrafast photoconductor, electron-hole pairs are generated which induce a photocurrent under an applied bias electric field. The induced photocurrent, which follows the envelope of the optical pump, drives the terahertz antenna connected to the photoconductor contact electrodes, generating terahertz radiation. The bandwidth of terahertz radiation is determined by the optical pulse, antenna characteristics, and semiconductor carrier lifetime. Since electrons have significantly higher mobilities compared to holes and the bias electric field increases non-linearly near the contact electrodes, the optical pump is focused onto the photoconductive gap asymmetrically close to the anode contact to

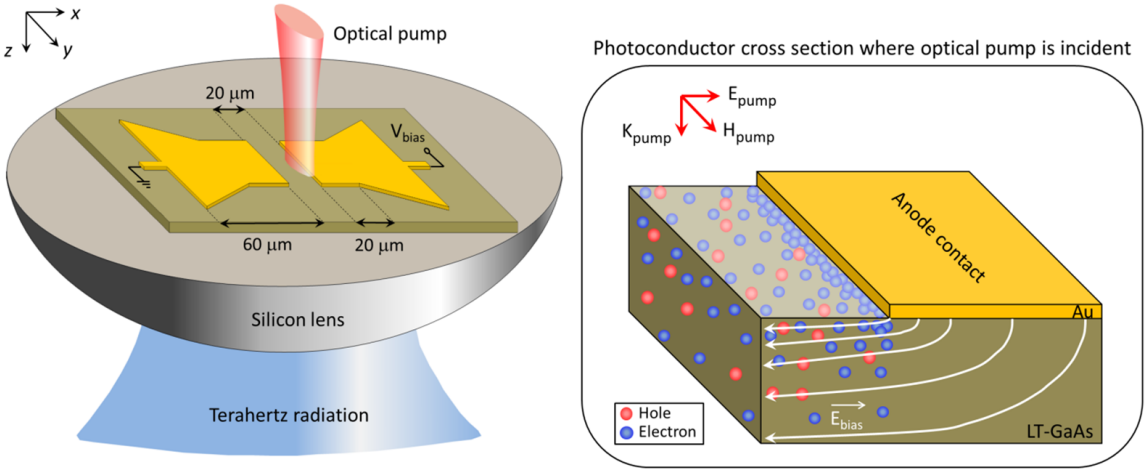

(a)

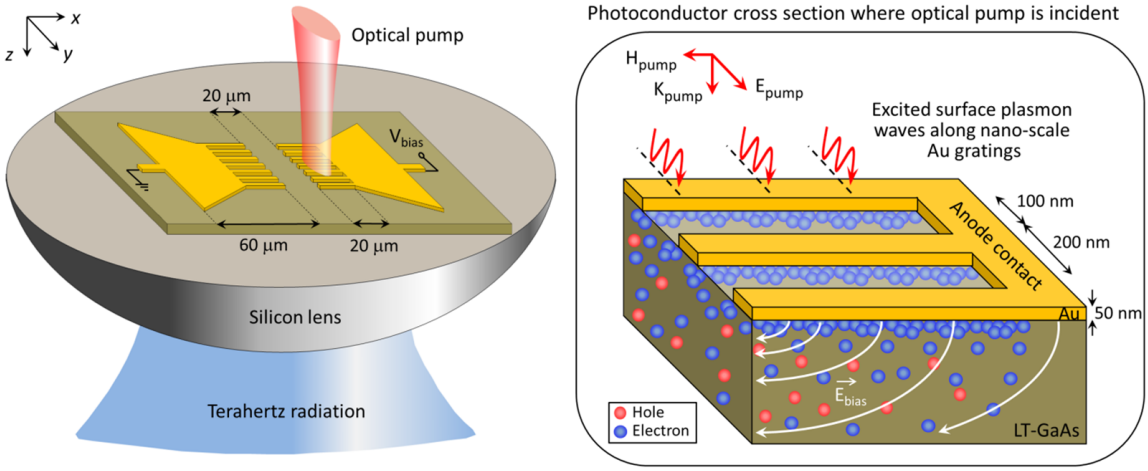

(b)

Figure 3.4: Schematic diagram and operation concept of photoconductive terahertz emitters. Left panels: an optical pump is incident upon an ultrafast photoconductor connected to a bowtie terahertz antenna on a LT-GaAs substrate. The device is mounted on a silicon lens to collect the terahertz radiation from back side of the substrate. Right panels: the incident optical pump generates electron-hole pairs in the substrate. Electron-hole pairs are separated under an applied bias electric field and drifted toward anode and cathode contact electrodes, respectively. Upon reaching the contact electrodes, the photocurrent drives the terahertz antenna to produce radiation. (a) A conventional photoconductive terahertz emitter. (b) A plasmonic photoconductive terahertz emitter incorporating plasmonic contact electrodes to reduce carrier transport times to contact electrodes and, thus, increase the collected photocurrent driving the terahertz antenna.

maximize terahertz radiation [11–13]. Similar to any conventional photoconductive terahertz emitter, the quantum efficiency of the described photoconductive emitter is limited by the relatively long carrier transport path lengths to photoconductor contact electrodes. This is because of the relatively low drift velocity of carriers in the semiconductor [14]. Even if the pump is focused down to a diffraction-limited spot size next to the anode contact, only a small portion of the photo-generated electrons can reach the anode in a sub-picosecond timescale. The remaining majority of photo-generated carriers become trapped and recombine in the substrate before reaching the contact electrodes, without contributing to terahertz generation.

Figure 3.4b shows the schematic diagram of the implemented photoconductive emitter that incorporates 20 µm long plasmonic contact electrode gratings designed to enhance the quantum efficiency of the conventional photoconductive emitter (Fig. 3.4a). The grating geometry is designed to excite surface plasmon waves along the periodic metallic grating interface upon incidence of a TM-polarized optical pump [15, 16]. Excitation of surface plasmon waves allows transmission of a large portion of the optical pump through the nanoscale grating into the photo-absorbing substrate. It also significantly enhances the intensity of the optical pump in close proximity to Au electrodes. As a result, the average photo-generated electron transport path length to the anode electrode is significantly reduced in comparison with the conventional photoconductive emitter (Fig. 3.4a). Therefore, the design strategy for the optimum plasmonic grating is maximizing the optical pump transmission into the photo-absorbing substrate while minimizing the electrode spacing to minimize the average photo-generated electron transport path length to the anode electrode.

Incorporating a dielectric passivation layer could reduce the Fresnel reflection at the semiconductor interface and, thus, could enhance optical pump transmission into the photo-absorbing semiconductor for both conventional and plasmonic photoconductors [17, 18]. While optical pump transmission into the photo-absorbing semicon-

ductor of the conventional photoconductor is the result of direct interaction between the pump wave and the semiconductor interface, optical pump transmission into the photo-absorbing semiconductor of the plasmonic photoconductor is through coupling to the excited surface plasmon waves. Because of the differences between the nature of the interacting waves with the semiconductor interface, the optimum passivation layer thicknesses that maximizes the transmission of the optical pump into the photo-absorbing semiconductor may not be not the same for the conventional and plasmonic photoconductors. While the passivation layer thickness can be independently optimized for each photoconductor, we have chosen the passivation layer thicknesses such that the same optical pump transmission into the photo-absorbing semiconductor can be achieved for conventional and plasmonic photoconductors that are fabricated on the same chip and under the same conditions. We used 150 nm SiO_2 passivation layer for the plasmonic photoconductor with 200 nm pitch, 100 nm spacing, and 50 nm height Au contact gratings and no passivation layer for the conventional photoconductor, which offer ∼70% optical pump transmission into the photo-absorbing semiconductor for both photoconductors at 800 nm optical pump wavelength.

3.2.1.1 Analytical Modeling

Using a finite element solver (COMSOL), we have analyzed the interaction of an incident optical pump (λ = 800 nm) with the conventional and plasmonic photoconductors. For maximum optical power enhancement near photoconductor contact electrodes, we have aligned the optical pump field along the x-axis and y-axis for the conventional and plasmonic photoconductors, respectively [19]. The optical absorption in the semiconductor substrate for the conventional (xz cross section) and plasmonic (yz cross section) photoconductors is shown in Fig. 3.5a.

For the conventional photoconductor, the metal contact shadows the substrate from the incident optical pump, allowing for almost all of the optical absorption and

photocarrier generation in the gap between the anode and cathode. In the case of the plasmonic photoconductor, the optical pump is transmitted through the nanoscale metallic grating through the coupling with surface plasmons. Since the excited surface plasmon waves exist at the dielectric-metal interface, the highest optical absorption and photocarrier generation occurs in direct proximity to the metal contacts. To better illustrate the impact of the excited surface plasmon waves, we have compared the optical absorption profile in the semiconductor substrate of the photoconductor with nanoscale Au gratings with a similar photoconductor with nanoscale Ni gratings. Although optical transmission can be obtained for the subwavelength Ni gratings, there is a large momentum mismatch between a surface plasmon wave on the Ni-GaAs interface at an 800 nm wavelength and the momentum available from the gratings. This makes the coupling of the incident light to a surface plasmon mode inefficient for the Ni grating. Figure 3.5a shows the optical absorption and photocarrier generation rates in the photoconductors, with the plots scaled to represent the same optical transmission into the substrates. From the figure, the highest optical absorption and photocarrier generation regions are more tightly confined at the metal-semiconductor interface of Au gratings in comparison with Ni gratings.

Using COMSOL, we have analyzed the bias electric field that drifts photocarriers toward the photoconductor contact electrodes (Fig. 3.5b). For this analysis, the bias voltage is set such that the maximum induced electric field remains below 10^5 V/cm (1/4 of the GaAs breakdown electric field). In the case of the conventional photoconductor, we see elliptical electric field lines beneath the contact electrode with the highest electric field near the corner of the electrodes. In the case of the plasmonic photoconductor, the electric field lines are illustrated at the yz cross section 1 μm away from the grating tip. Although relatively lower electric fields are induced in the case of the plasmonic photoconductor compared with the conventional photoconductor, the electric field levels are maintained above 10^3 V/cm (at which electron drift velocity

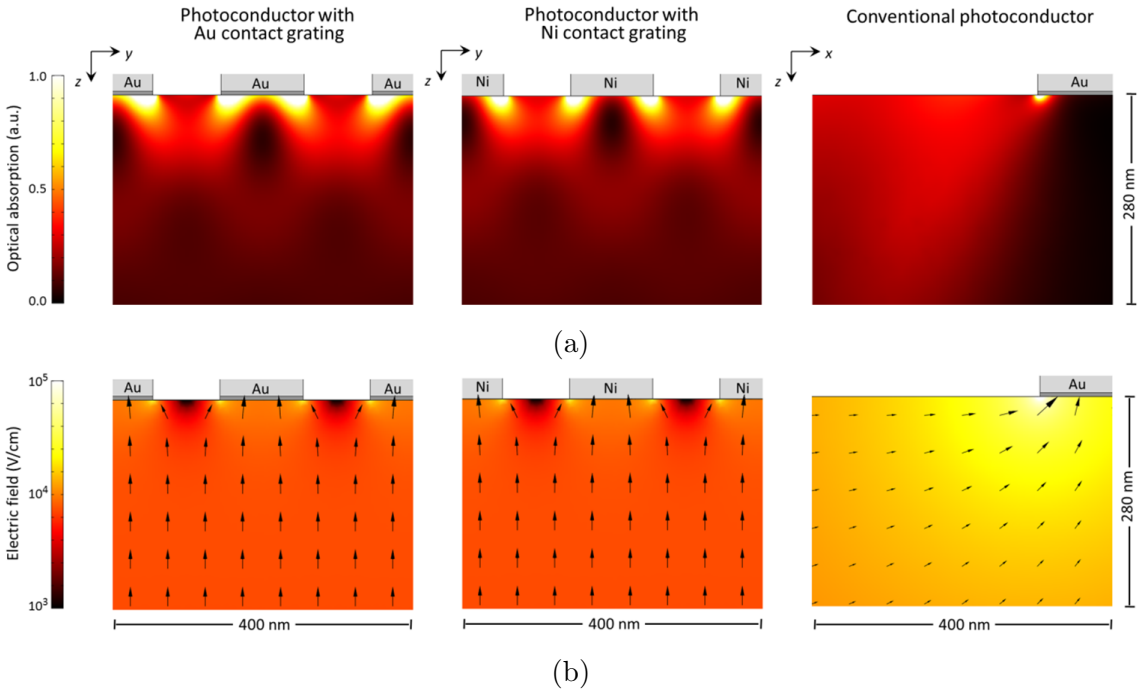

Figure 3.5: Finite element analysis of optical and electrical interactions in the photoconductor cross sections. Right panel: cross section of the conventional photoconductor (xz-plane), Left panels: cross sections of the designed plasmonic photoconductor and a similar photoconductor with Ni contact gratings (yz-plane). A 5 nm thick Ti adhesion layer is deposited under Au electrodes. A 150 nm thick SiO_2 passivation layer is used for the photoconductors with nanoscale contact gratings and no passivation layer is used for the conventional photoconductor. This allows equal optical transmission to the photo-absorbing substrate ($\sim$70%) at 800 nm optical pump wavelength for all three photoconductors. (a) Color plot of optical absorption in GaAs substrate due to an incident optical plane wave (λ = 800 nm). The optical pump field is aligned along the x-axis and y-axis for the conventional photoconductor and photoconductors with nanoscale contact gratings, respectively. (b) Bias electric field in GaAs substrate. Color map corresponds to electric field magnitude, and arrows denote field direction. Applied voltages in all three cases are set to not exceed electric fields of 1×10^5 V/cm. The cross sections of the photoconductors with nanoscale contact gratings are shown for a distance 1 µm inset from the tip of the gratings.

reaches saturation) within 100 nm from photoconductor anode contact electrodes [14]. Moreover, simulation results show that the electric field levels are maintained above 10^3 V/cm within 100 nm from contact electrodes along a 20 µm long plasmonic contact electrode, indicating that the superior performance of the plasmonic photoconductive emitter can be maintained when using relatively large device active areas.

The impulse response of the analyzed photoconductors to an optical pump impulse is estimated by calculating the collected transient photocurrent at the contact electrodes using a multi-physics finite-element solver (COMSOL). For this purpose, the photogenerated carrier density is derived from the calculated optical intensity in the GaAs substrate and combined with the electric field data in the classical drift-diffusion model to calculate the induced photocurrent. The results are presented in Fig. 3.6a, indicating the superior performance of the designed plasmonic photoconductor offering high-quantum efficiency and ultrafast operation simultaneously. The advantage of the designed plasmonic photoconductor is more apparent when comparing its responsivity with the conventional photoconductor and the photoconductor with Ni contact gratings. The responsivity spectra are calculated by convolving the impulse response of the analyzed photoconductors with the sinusoidal power envelope of two frequency-offset optical beams as a function of optical beat frequency. The responsivity spectra (Fig. 3.6b) show that the designed plasmonic photoconductor offers more than one order of magnitude higher responsivity levels compared with the conventional photoconductor. Moreover, comparing the responsivity spectra of the designed plasmonic photoconductor with the photoconductor with Ni contact gratings indicates the impact of plasmonic optical enhancement in direct proximity to the metal contacts, which offers higher photoconductor responsivity levels especially at higher terahertz frequencies. It should be mentioned that at a given pump power, the radiated power from a photoconductive emitter has a quadratic dependence on the photoconductor responsivity. Therefore, compared with the conventional photo-

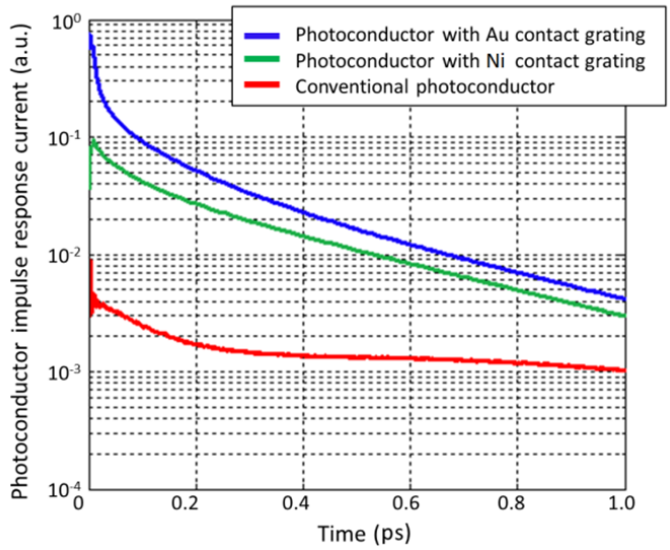

(a)

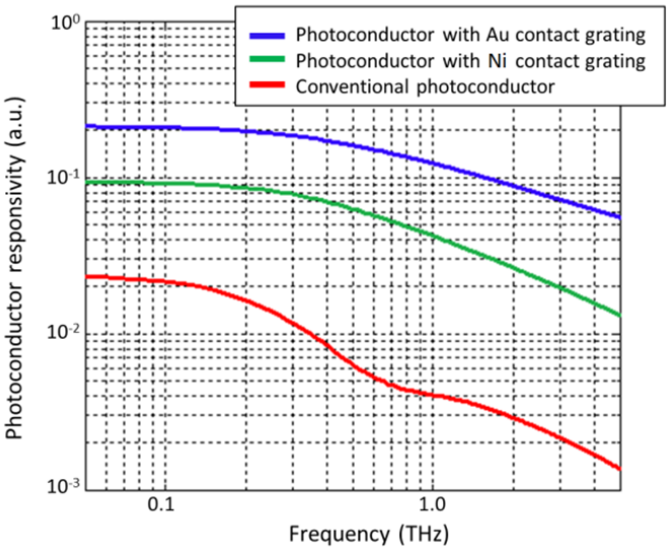

(b)

Figure 3.6: Impulse response and AC responsivity of photoconductors. (a) Estimated impulse response of the analyzed photoconductors with the illustrated cross sections by combining the photogenerated carrier density in the GaAs substrate, the electric field data, and the classical drift-diffusion model in a multi-physics finite-element solver (COMSOL). The induced photocurrent in response to an optical pump impulse is calculated. A carrier lifetime of 400 fs is assumed for the LT-GaAs substrate. (b) Estimated responsivity spectra of the analyzed photoconductors calculated by convolving the impulse response of each photoconductor with the sinusoidal power envelope of two frequency-offset optical beams as a function of optical beat frequency.

conductor, the designed plasmonic photoconductor is expected to offer two orders of magnitude higher optical-to-terahertz conversion efficiencies.

3.2.2 Methods

3.2.2.1 Fabrication

Figure 3.7 shows the microscope and SEM images of the fabricated photoconductive emitter prototypes. Fabrication began with the patterning of the nanoscale gratings using electron beam lithography, followed by Ti/Au (5/45 nm) deposition and lift-off to form ohmic photoconductor contacts [20]. A 150 nm thick SiO_2 passivation layer was then deposited using PECVD. Using a plasma etcher, contact vias were then opened, and the antenna and metal contacts were formed using optical lithography followed by Ti/Au (5/400 nm) deposition and lift-off. Complete fabrication details are listed in Appendix A. The fabricated devices were then mounted on a silicon lens and placed on an optical rotation mount for optical pump polarization adjustments.

3.2.2.2 Radiation Power Measurement

In performing terahertz radiation power measurements, the beam from a mode-locked Ti:sapphire laser (800 nm central wavelength, 76 MHz repetition rate, 200 fs pulse width, 5 Hz amplitude modulation) is tightly focused onto the active area of the device under test. The device, mounted on an optical rotation mount and held by an XYZ translation stage, is positioned to maximize the radiated power. For optimal performance of the conventional terahertz emitter, the incident optical electric field is oriented to span the anode-cathode gap. The metal gratings of the plasmonic terahertz emitter are likewise oriented to run perpendicular to the incident electric field, for best performance. A parametric analyzer is used to simultaneously apply bias voltages and measure the electrical current drawn. Emitted radiation is

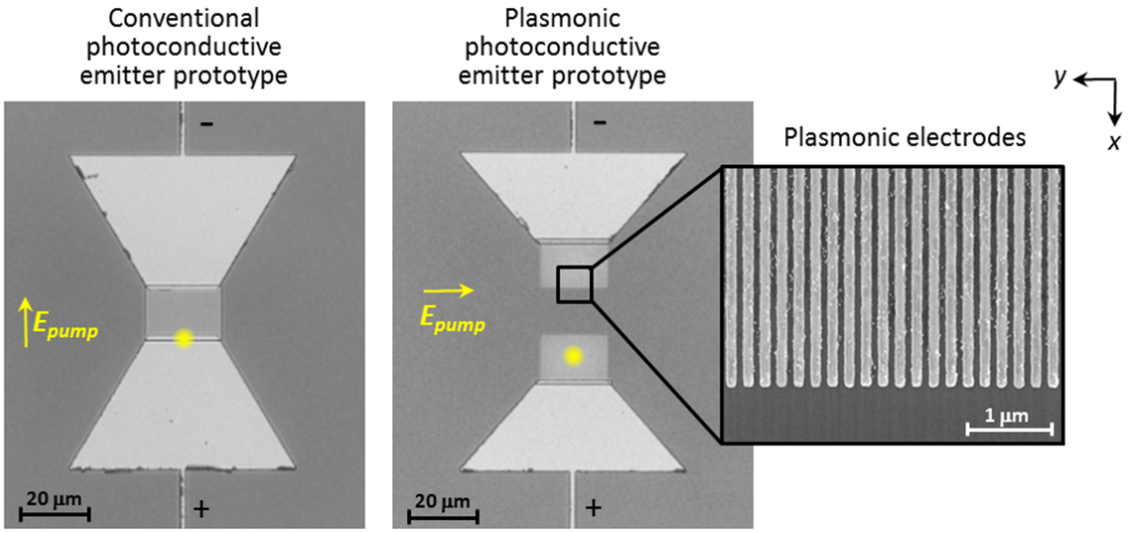

Figure 3.7: Fabricated bowtie emitter images. Left: microscope image of the conventional terahertz emitter. Middle: microscope image of the plasmonic terahertz emitter. Right: SEM image of the plasmonic electrodes of the plasmonic terahertz emitter. The circular pump spot is positioned on the antenna axis at the anode contact edge and along the anode plasmonic contact electrodes for the conventional and plasmonic photoconductive emitters, respectively.

measured using a pyroelectric detector (Spectrum Detector, Inc. SPI-A-65 THz) and converted to terahertz power using the manufacturer's responsivity values.

3.2.2.3 Radiation Spectral Characterization

Emitted terahertz power is monitored in the time-domain and frequency-domain through a terahertz time-domain spectroscopy setup using electro-optic sampling [21]. The setup uses the same Ti:sapphire laser used in the power measurements with the pump path amplitude modulated at 2 kHz. The pump beam is focused onto the device under test, and the emitted radiation is collimated and focused using two polyethylene spherical lenses in the ambient atmosphere. Before the focal point of the second polyethylene lens, the terahertz radiation is combined with the optical pump beam using an ITO coated glass filter. Both paths are then focused onto a 1 mm thick, <110> ZnTe crystal. The optical beam is then converted into circular polarization, separated by a Wollaston prism, and measured using two balanced

detectors connected to a lock-in amplifier.

3.2.3 Experimental Results

To evaluate the performance of the photoconductive terahertz emitter with and without the plasmonic gratings, the output power of each device was measured, using a pyroelectric detector (Spectrum Detector, Inc. SPI-A-65 THz), in response to an incident optical pump from a Ti:sapphire mode-locked laser with a central wavelength of 800 nm, 76 MHz repetition rate, and 200 fs pulse width. In order to maximize terahertz radiation, the incident optical pump was tightly focused onto each device and positioned on the antenna axis at the anode contact edge and along the anode plasmonic contact electrodes for the conventional and plasmonic photoconductive emitters, respectively, as illustrated in Fig. 3.7. The device rotation mount was adjusted to align the electric field of the optical pump along the x-axis and y-axis for the conventional and plasmonic prototypes, respectively.

The measured output power of the two prototype devices at a 40 V bias voltage and under various optical pump powers is presented in Fig. 3.8a. A radiation power enhancement of more than 33 was observed from the plasmonic photoconductive emitter in the 0 - 25 mW optical pump power range. This significant radiation power enhancement is due to the higher photocurrent levels generated when employing plasmonic contact electrodes (Fig. 3.8a inset), which have a quadratic relation with the radiation power. Another important advantage of the plasmonic emitter is that the close proximity of the photocarriers to the contact electrodes is satisfied over significantly larger device active areas, and thus, the operation of the plasmonic emitter is more tolerant to optical pump misalignment. While the radiated power from the conventional emitter drops dramatically as a result of optical pump displacement along the x-axis, the plasmonic emitter exhibits a less significant drop in power as a result of the optical pump displacement along the 20 µm long anode plasmonic contact

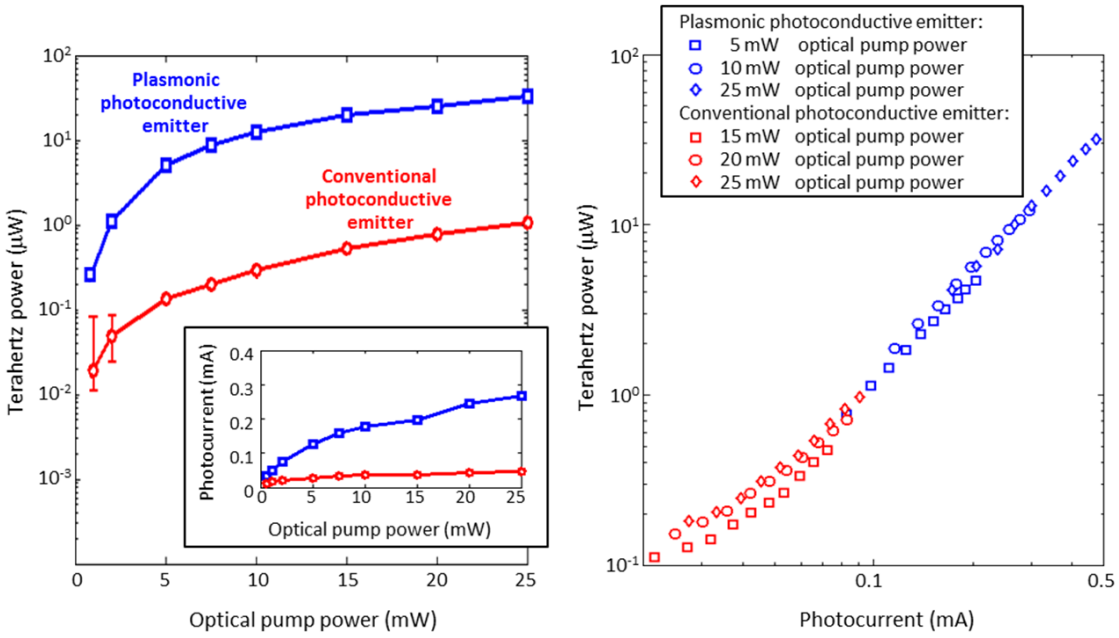

(a) (b)

Figure 3.8: Radiated power of bowtie photoconductive terahertz emitters. (a) Measured terahertz radiation from the plasmonic and conventional terahertz sources, electrically biased at 40 V, under various optical pump powers. The inset curve shows the corresponding photocurrent. The error bars are associated with the noise of the pyroelectric terahertz detector listed in the detector datasheet. (b) Measured terahertz radiation versus collected photocurrent for the plasmonic and conventional terahertz emitters. The data represented in the plot includes various bias voltages (10 - 40 V) under various optical pump powers (5 - 25 mW).

electrodes.

To further examine the impact of photocurrent increase on the radiation power enhancement, we compared the radiation power of the two photoconductor devices as a function of their photocurrent under various bias voltages (10 - 40 V) and optical pump powers (5 - 25 mW). The results are presented in Fig. 3.8b in a logarithmic scale. The data points are all curve-fitted to the same line with a slope of 2, confirming the quadratic dependence of the radiation power on the induced photocurrent and the fact that all other operational conditions (including antenna specifications) are the same for the conventional and plasmonic photoconductive emitter prototypes.

By dividing the output power of the plasmonic photoconductive emitter by the

output power of the conventional photoconductive emitter, we define a power enhancement factor. Figure 3.9a shows the power enhancement factor under various optical pump powers and bias voltages. At low optical pump power levels and a bias voltage of 30 V, output power enhancement factors up to 50 are observed, the same order of magnitude predicted by the theoretical predictions. The enhancement factor decreases slightly at higher optical pump power levels. This can be explained by the carrier screening effect, which affects the plasmonic photoconductor more than the conventional photoconductor, since a larger number of electron-hole pairs are separated in the plasmonic photoconductor. Additionally, the enhancement factor decreases slightly at higher bias voltages. This is because stronger forces separate electron-hole pairs at higher bias voltages. Since a larger number of electron-hole pairs contribute to the induced photocurrent in the plasmonic photoconductor, the relative increase in the induced electric field opposing the bias electric field is higher. It should be also mentioned that the lower enhancement factors at bias voltages below 30 V are associated with insufficient bias electric field levels along the electrodes of the plasmonic photoconductor.

Finally, the maximum radiated power from each photoconductive terahertz emitter was measured at an optical pump power of 100 mW, up to the point that the devices burned, as shown in Fig. 3.9b. At maximum, the plasmonic photoconductive emitter produced an average power of 250 µW, compared to the 12 µW of the conventional photoconductive emitter.

The time-domain (Fig. 3.10a) and frequency-domain (Fig. 3.10b) radiation of the plasmonic photoconductive emitter in response to a 200 fs optical pump pulse from the Ti:sapphire mode-locked laser was measured using a terahertz time-domain spectroscopy setup with electro-optic detection [22]. The radiated power from the plasmonic terahertz source was detected up to 1.5 THz, after which the noise of the system limited detection. The observed radiation peaks around 0.35 THz and 0.55

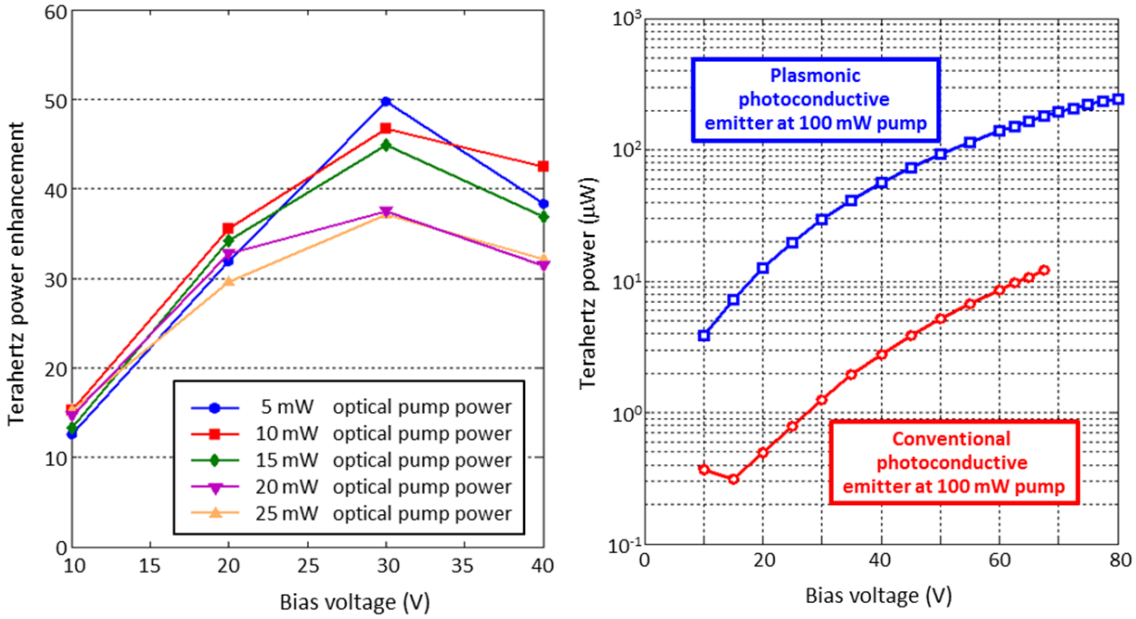

(a) (b)

Figure 3.9: Radiation performance of bowtie photoconductive terahertz sources. (a) Relative terahertz power enhancement defined as the ratio of the terahertz power emitted by the plasmonic terahertz emitter to the conventional terahertz emitter. Maximum enhancement is obtained at low optical powers before the onset of the carrier screening effect. (b) Maximum terahertz power measured from the plasmonic and conventional terahertz emitters under a 100 mW optical pump. The bias voltage of each device is increased until the point of device failure.

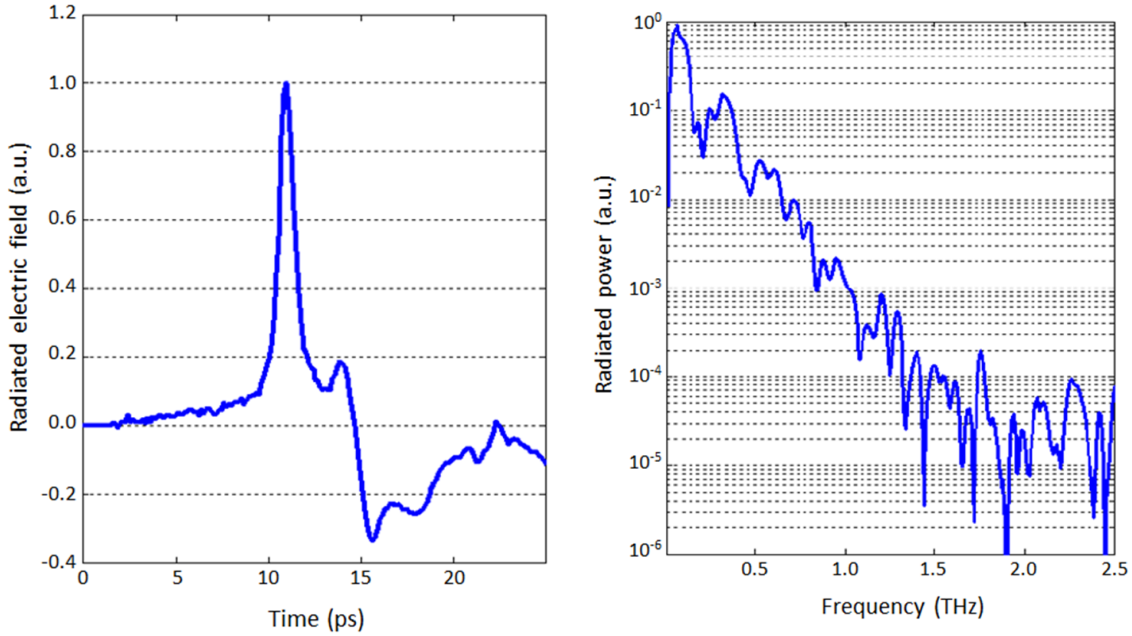

(a) (b)

Figure 3.10: Radiated electric field of the plasmonic photoconductive terahertz source in the (a) time-domain and (b) frequency-domain.

THz are associated with the resonance peaks of the employed bowtie antenna and the radiation peak around 0.1 THz is associated with the resonance peak of the dipole antenna formed by the bowtie antenna bias lines. The detailed description of the terahertz time-domain spectroscopy setup can be found in the methods section.

3.2.4 Improving Radiated Power Using Broadband Antennas

In the previous section, a bowtie antenna is used to demonstrate the radiation enhancement that plasmonic electrode based photoconductive terahertz sources can offer over conventional sources. Plasmonic electrodes can, however, be integrated with almost any other type of terahertz antenna and optimized for various performance requirements. When operating in pulsed mode, since the antenna is being driven by a broadband pulse of electrical current, the ideal antenna should be chosen to offer a large broadband radiation resistance while maintaining a reactance near 0 Ω. We designed a logarithmic spiral antenna integrated with plasmonic electrodes for

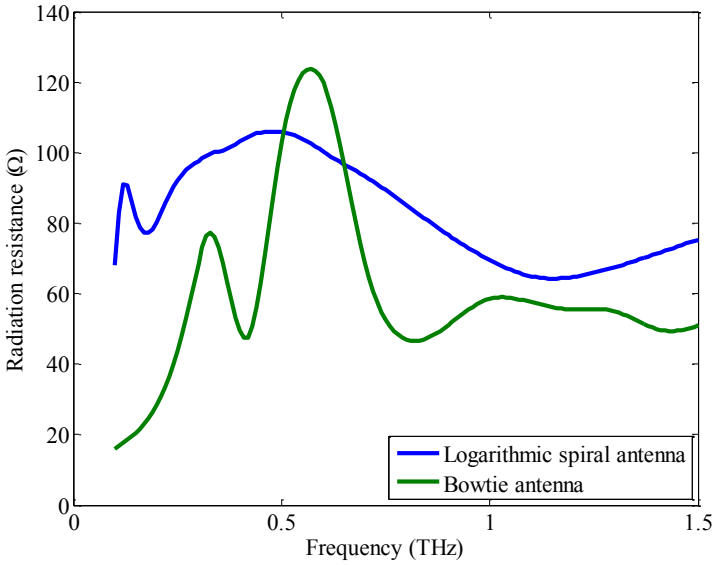

Figure 3.11: Radiation resistance of logarithmic spiral and bowtie antennas.

efficient terahertz generation over a broad frequency range.

The logarithmic spiral antenna is designed to offer a broadband radiation resistance of ∼70-100 Ω over the 0.1-1.5 THz range, as shown in Fig. 3.11. Each contact electrode of the plasmonic photoconductive emitter is a plasmonic grating covering a 30×30 µm^2 area. The relatively large active area allows the optical pump to be spread to decrease the carrier screening effect. The end-to-end spacing between the anode and cathode contact electrodes is 30 µm to maintain a large resistance between the anode and cathode contacts. The plasmonic contact electrode gratings (pitch = 225 nm, metal width = 125 nm, metal height = 50 nm) are designed to maximize device quantum efficiency at optical pump wavelength of 800 nm [23, 24].

3.2.4.1 Experimental Results

The designed terahertz emitter is fabricated on a LT-GaAs substrate. Figure 3.12 shows the microscope image of the fabricated plasmonic photoconductive emitter and the scanning electron microscope (SEM) image of the plasmonic contact electrodes. Details of the fabrication process are listed in Appendix B. The emitter is charac-

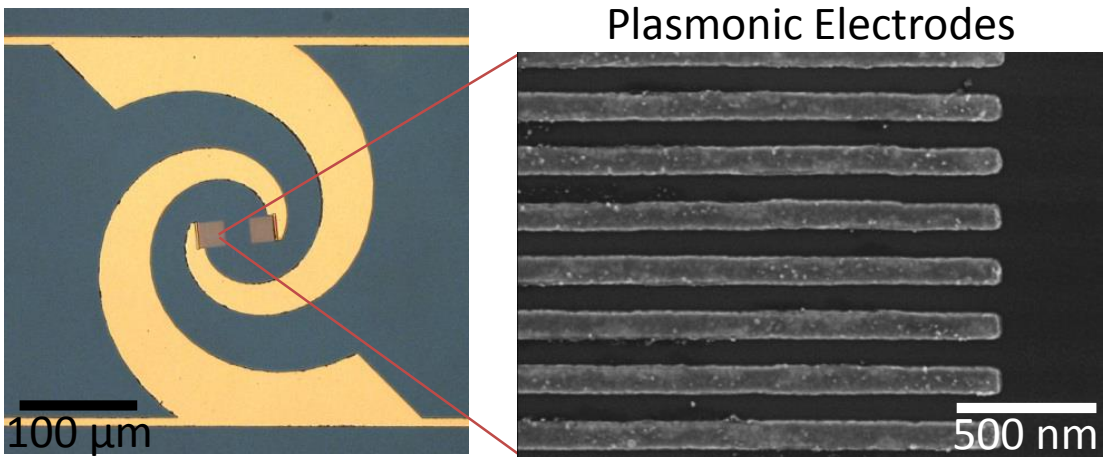

Figure 3.12: Fabricated logarithmic spiral antenna integrated with plasmonic electrodes. Left: Microscope image of the spiral antenna. Right: SEM image of the plasmonic electrodes

terized in response to a 200 fs optical pump, which is focused asymmetrically on the anode plasmonic electrode [11–13].

The radiated electric field of the plasmonic photoconductive source is characterized in a time-domain spectroscopy setup with electro-optic detection in a 1 mm thick ZnTe crystal. The measured time-domain and frequency-domain radiation are shown in Fig. 3.13a and 3.13b, respectively. In the time-domain plot (Fig. 3.13a), it is worth noting that the pulse is visibly chirped. This is a result of the spiral shape of the antenna, which is a traveling wave antenna that efficiently radiates wavelengths equal to 2π times the instantaneous radius [25]. As a result, as the pulse of current propagates from the center of the spiral outward, higher frequency components are radiated first. The frequency domain plot (Fig. 3.13b) indicates a radiation bandwidth of 2 THz.

The radiated power is measured as a function of the optical pump power and bias voltage (Fig. 3.14) using a pyroelectric detector. With an optical pump power of 20 mW, a single emitter element produces 100 µW of terahertz power at a bias voltage of 40 V, ∼4 times higher than the radiated power offered by the plasmonic photoconductive emitter based on the bowtie antenna.

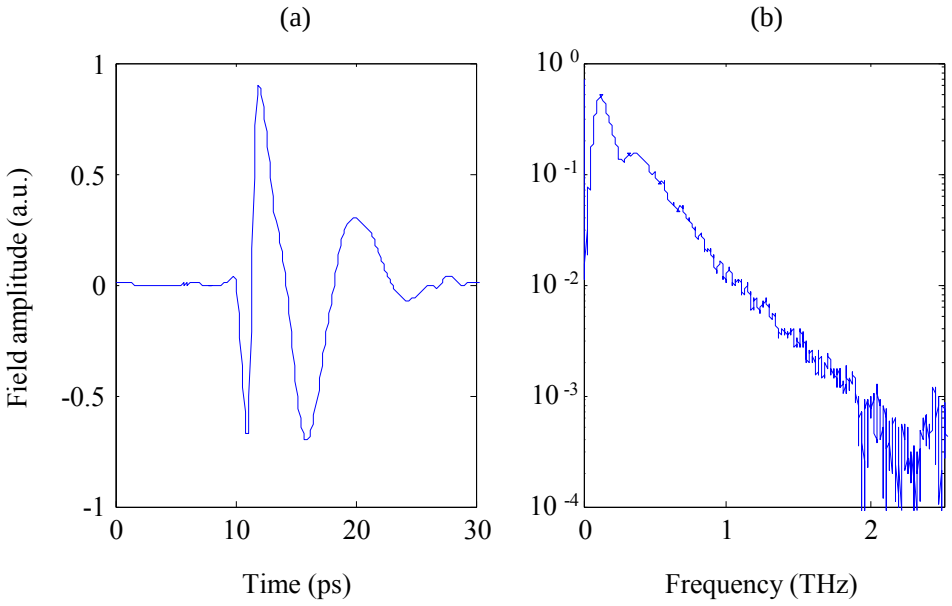

Figure 3.13: Measured electric field in the (a) time-domain and (b) frequency-domain.

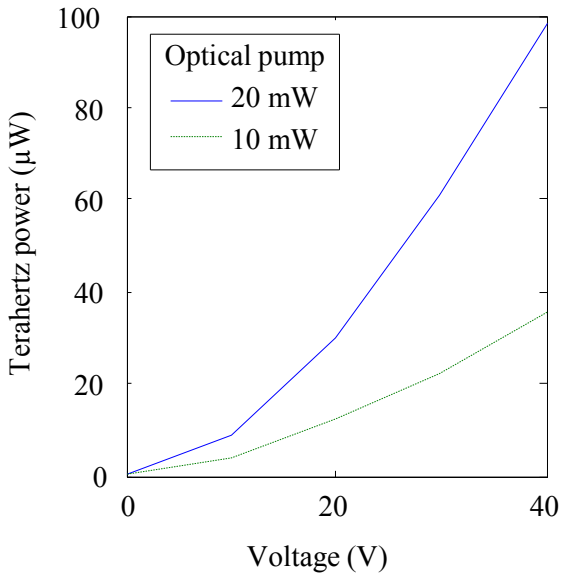

Figure 3.14: Radiated power from the logarithmic spiral photoconductive terahertz source with plasmonic electrodes.

3.2.5 Utilizing Antenna Arrays for High Output Power

To accommodate applications requiring terahertz powers exceeding what can be offered by a single photoconductive terahertz antenna, we designed and implemented a two dimensional array of photoconductive terahertz emitters based on a logarithmic spiral antenna array that incorporates plasmonic contact electrodes. This design further increases the maximum terahertz radiation power levels by not only extending the antenna bandwidth, but also by mitigating the carrier screening effect at high optical pump powers. Under a 400 mW optical pump power, the emitter generates 1.9 mW of terahertz radiation in the 0.1-2 THz range.

Figure 3.15a shows the schematic diagram of the presented terahertz emitter, which consists of a 3×3 array of plasmonic photoconductive emitters with logarithmic spiral antennas. A microlens array is used to simultaneously split and focus portions of the optical pump beam onto the active area of each plasmonic photoconductive emitter in the 3×3 array. For efficient optical focusing, the pitch of the antenna array is designed to match that of the microlens array at 500 µm. The logarithmic spiral antennas and plasmonic contacts are identical to those in Section 3.2.4, offering a broadband radiation resistance of ∼70-100 Ω over the 0.1-2 THz range and efficient optical pump transmission through the plasmonic electrodes into the photo-absorbing semiconductor.

The designed terahertz emitter is fabricated on a LT-GaAs substrate. Figure 3.15b shows the microscope image of the fabricated plasmonic photoconductive emitter and the scanning electron microscope (SEM) image of the plasmonic contact electrodes.

To excite the 3×3 plasmonic photoconductive emitter array, the microlens array is mounted on a motorized rotation mount. The fabricated plasmonic photoconductive emitter is mounted on a motorized XYZ translation stage for precise alignment, and the optical alignment of the microlens and terahertz emitter array is optimized iteratively using computer control.

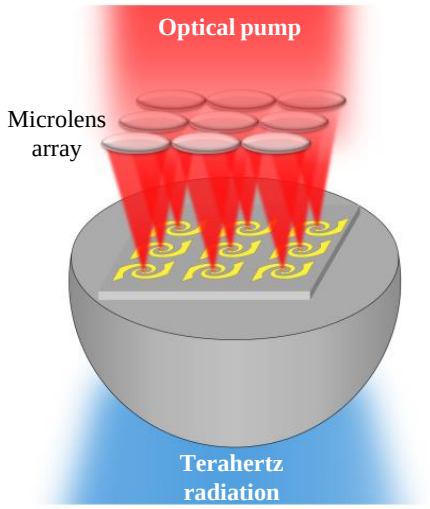

(a)

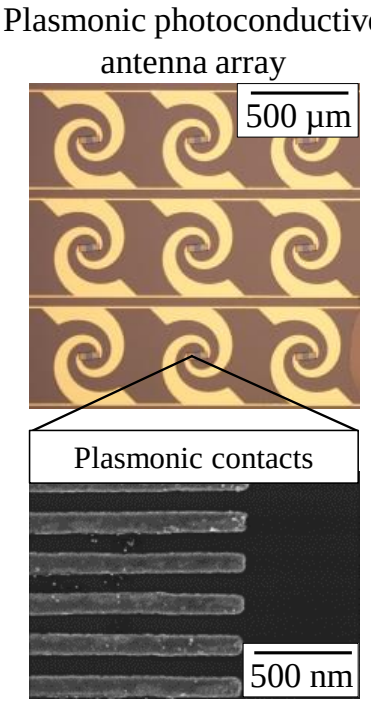

(b)

Figure 3.15: Plasmonic photoconductive terahertz emitter array. (a) Schematic. A microlens splits and focuses the optical pump beam onto the active area of each terahertz emitter element. The emitter array is mounted on a hyper-hemispherical silicon lens through which the terahertz radiation emits. (b) Fabricated emitter array.

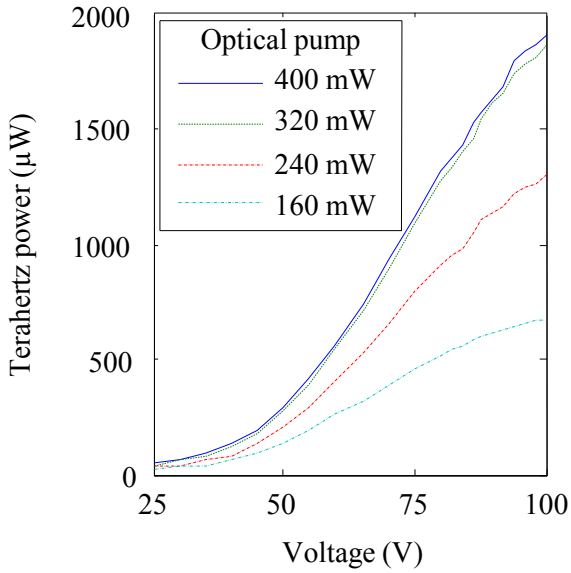

Figure 3.16: Radiated power from a 3×3 plasmonic photoconductive emitter array.

The radiated power of the plasmonic photoconductive emitter array is shown in Fig. 3.16b. Up to 1.9 mW of terahertz power is measured at 400 mW optical pump power and bias voltage of 100 V. It should be noted that at high terahertz powers the output of the pyroelectric detector saturates. To measure terahertz powers above ∼1 mW, a terahertz attenuator is inserted before the pyroelectric detector and the measured power is scaled according to the change in the pyroelectric detector's measured signal. Since the incident optical pump beam on the microlens array has a Gaussian spatial profile, the optical power incident upon the center device in the array is significantly higher than that of the surrounding devices. By only applying the bias voltage to the center 1×3 plasmonic photoconductive emitter array, we observe that approximately 50% of the total emitted power from the 3×3 plasmonic photoconductive emitter array is generated by the middle row of the array. The radiation power and optical-to-terahertz conversion efficiency of the presented plasmonic photoconductive emitter array can be enhanced even further by increasing the overall array size and/or using a diffuser before the microlens array to distribute the optical pump power more evenly across the emitter elements.

3.2.6 Discussion

The ability to excite surface plasmon waves has enabled many unique opportunities for routing and manipulating electromagnetic waves [26]. It has enabled strong light concentration in the near-field paving the way for higher resolution imaging and spectroscopy [27, 28], deep electromagnetic focusing and beam shaping [29, 30], higher efficiency photovoltaics [31, 32], photodetectors [33, 34], modulators [35, 36], and photoconductors [37]. On the basis of this capability, we have proposed and experimentally demonstrated up to 50 times radiation power enhancement by incorporating plasmonic contact electrodes in a photoconductive terahertz emitter. Plasmonic electrodes are designed to significantly reduce the average carrier transport

distance to photoconductor contact electrodes over relatively large device active areas and without a considerable increase in the capacitive loading to the terahertz radiating antenna. This enables boosting the maximum terahertz radiation power [38–43] by mitigating the carrier screening effect [44], semiconductor bleaching [45], and thermal breakdown [46] at high optical pump powers.

It should be noted that the focus of this study has been the demonstration of the impact of plasmonic electrodes in enhancing the induced photocurrent in ultrafast photoconductors and the radiated terahertz power from photoconductive terahertz emitters. Thus, the choice of the photoconductive emitter architectures, terahertz radiating antennas, and bias feeds in this study are not exhaustive. The enhancement concept can be similarly applied to enhance the radiation power from photoconductive terahertz emitters with a variety of terahertz antennas with and without interdigitated contact electrodes as well as large-area photoconductive terahertz emitters in both pulsed and continuous-wave operation. In this regard, the output power of our prototype devices can be further enhanced through use of resonance cavities [12, 15] and antennas with higher radiation resistance and bandwidth [47, 48]. Moreover, the use of high aspect ratio plasmonic contact electrodes embedded inside the photo-absorbing semiconductor [49, 50] allows a larger number of carriers generated in close proximity with photoconductor contact electrodes and, thus, enables further terahertz radiation enhancement. In this regard, extending the plasmonic electrode height to dimensions larger than the optical pump absorption depth allows ultrafast transport of the majority of photocarriers to the photoconductor contact electrodes and their efficient contribution to terahertz generation. This eliminates the need for using short carrier lifetime semiconductors, which are used for suppressing the DC current of photoconductive emitters (in general) and for preventing undesired destructive interferences in continuous-wave photoconductive emitters (in specific) [24]. Eliminating the need for using short carrier lifetime semiconductors, which have

lower carrier mobilities and thermal conductivities [46] compared to high quality crystalline semiconductors, would have an important impact on future high power and high efficiency photoconductive terahertz emitters.

3.3 Broadening Substrate Compatibility

One of the important advantages of the plasmonic photoconductive terahertz source architecture is that it can eliminate the need for short-carrier lifetime photo-absorbing substrates which are necessary in conventional photoconductive terahertz sources. By incorporating plasmonic contact electrodes, the average photo-generated carrier transport path to the photoconductor contact electrodes is significantly reduced compared to conventional photoconductors with micron-scale contact electrode spacings. We experimentally demonstrate that the nanoscale carrier transport path lengths provided by plasmonic contact electrodes allow sub-picosecond photoconductor response time without using any short-carrier lifetime semiconductor. This enables high quantum efficiency and ultrafast operation simultaneously and paves the way toward high optical-to-terahertz conversion efficiencies.

3.3.1 Design

Figure 3.17 shows the schematic diagram and operation concept of a plasmonic photoconductive terahertz emitter based on a long-carrier lifetime semiconductor (Fig. 3.17b) in comparison with a conventional photoconductive terahertz emitter based on a short-carrier lifetime semiconductor with a similar terahertz antenna (Fig. 3.17a). The anode and cathode contact of the photoconductor consist of two arrays of nanoscale metallic gratings connected to the input port of a dipole terahertz antenna. Normally, optical transmission through subwavelength metallic apertures is diffraction limited. However, the grating geometry can be specifically designed to allow efficient optical transmission through the subwavelength metallic gratings into the

photo-absorbing active region by excitation of surface plasmon waves along the periodic metallic grating interface [15]. Instead of using an interdigitated configuration for the anode and cathode contact gratings, the contact gratings are interconnected with an overall spacing of ∼3 µm between the anode and cathode contacts. This maintains low capacitive loading to the terahertz radiating antenna while reducing the photo-generated carrier transport path to the contact electrodes significantly. The shortcoming of the presented contact electrode configuration is that only half of the photo-generated carriers will reach the contact electrode gratings in a sub-picosecond time-scale, limiting the maximum photoconductor quantum efficiency to 50%. In order to maintain the ultrafast operation of the photoconductor in the absence of a short-carrier lifetime substrate, a middle ground electrode will collect the remaining holes and electrons and prevents their slow collection by the opposite anode and cathode contact electrodes. Conventional photoconductive terahertz emitters are usually fabricated on a ∼1 µm thick short-carrier lifetime semiconductor layer. Although only the photocarriers generated within ∼100 nm from the contact electrodes can be collected in a sub-picosecond time-scale to contribute to terahertz radiation, excess carriers generated deeper inside the substrate would not increase photoconductor DC current due to recombination before reaching photoconductor contact electrodes. In order to maintain low photoconductor DC current levels and a sub-picosecond device response time in the absence of a short-carrier lifetime substrate, the presented plasmonic photoconductive terahertz emitter is fabricated on a photo-absorbing semiconductor layer with less than 100 nm thickness to prevent photo-carrier generation at deep semiconductor regions that do not contribute to terahertz radiation.

Interaction of the optical pump with the nanoscale contact gratings is analytically characterized and the grating structure is designed to allow ultrafast and high quantum efficiency operation simultaneously [23]. Figure 3.18a shows the designed nanoscale Au grating with 200 nm pitch, 100 nm metal width, and 50 nm metal

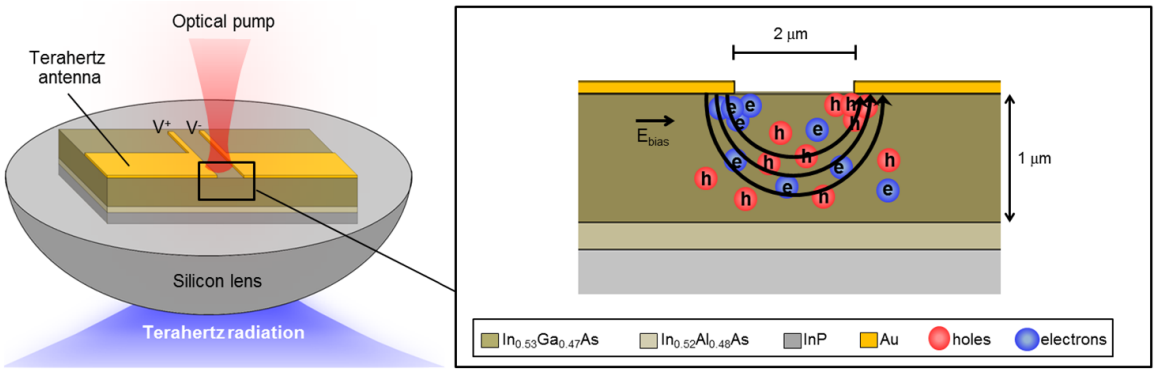

(a)

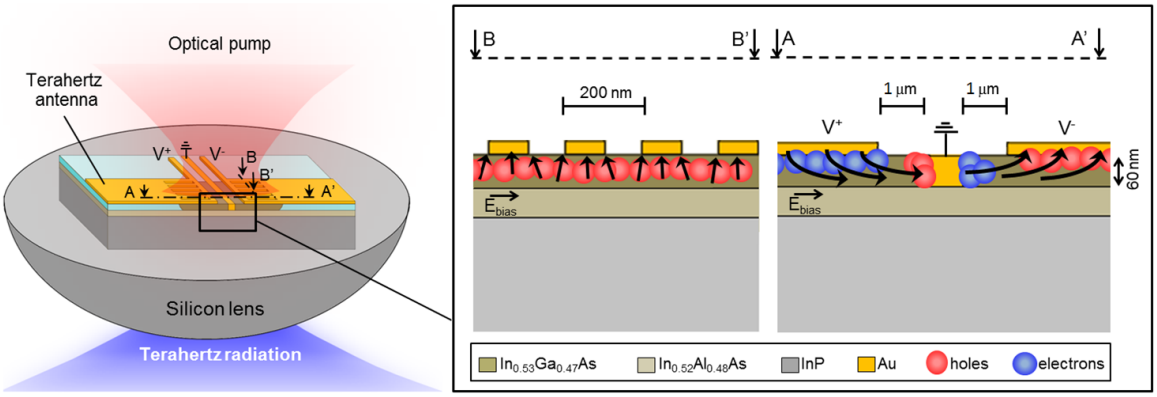

(b)

Figure 3.17: Schematic diagram and operation concept of conventional and plasmonic photoconductive terahertz emitters. (a) Conventional photoconductive terahertz emitters based on short-carrier lifetime photo-absorbing semiconductors. (b) Plasmonic photoconductive terahertz emitter based on nanoscale contact electrode gratings on a high-quality crystalline substrate.

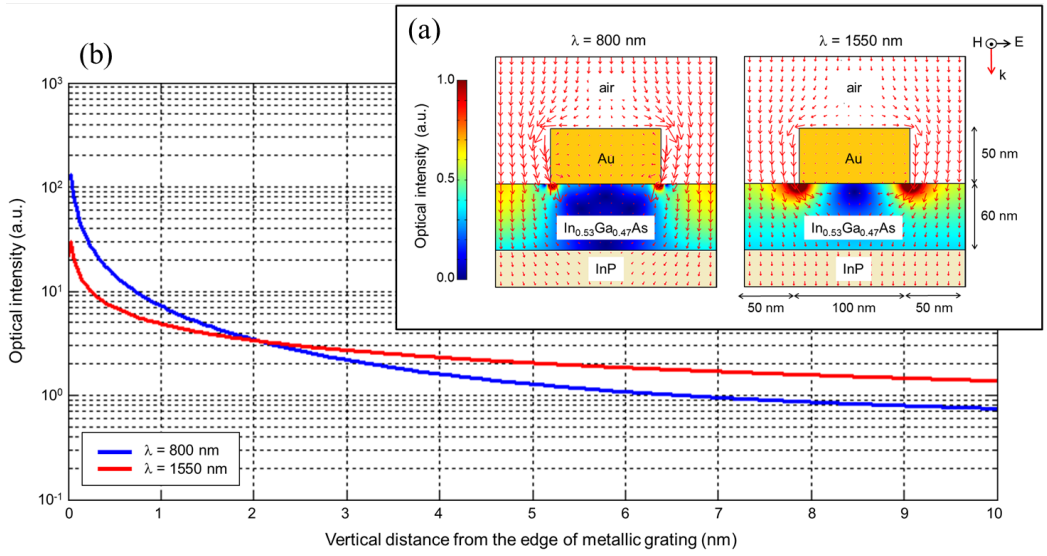

Figure 3.18: Interaction of an optical beam with subwavelength gratings. (a) A TM-polarized optical beam interacting with the designed Au grating at 800 nm and 1550 nm. Red arrows and color-map show the optical power flow and intensity inside the $In_{0.53}Ga_{0.47}As$ active layer, respectively. (b) Optical intensity variation as a function of vertical distance from the edge of Au gratings, indicating the tightly confined surface plasmon waves at the Au-$In_{0.53}Ga_{0.47}As$ interface.

height for enhanced transmission of a TM-polarized optical pump at 800 and 1550 nm wavelengths into a 60 nm $In_{0.53}Ga_{0.47}As$ active layer grown on a lattice-matched $In_{0.52}Al_{0.48}As$ buffer layer on a semi-insulating InP substrate. Using a finite-element solver (COMSOL), we have analyzed the interaction of a TM-polarized optical wave with the designed Au grating at 800 nm and 1550 nm wavelengths. The power flow (red arrows) at the Au grating cross section shows how the propagating light bends on top of the subwavelength metallic grating to allow high efficiency transmission into the photo-absorbing substrate. It also shows that the intensity of the transmitted optical pump is significantly enhanced near the corners of the Au grating, further reducing the average transport time of the photo-generated carriers to the contact electrodes. Optical intensity enhancement near the corners of the Au grating is due to the excitation of surface plasmon waves along the periodic Au grating interface, which are constrained at the metal-dielectric interface.

The designed nanoscale Au grating offers about 60% optical transmission into the

$In_{0.53}Ga_{0.47}As$ active layer at 800 nm and 1550 nm, bound by the Fresnel reflection at the $In_{0.53}Ga_{0.47}As$ -air interface. However, the optical intensity in close proximity to the Au gratings is about an order of magnitude higher at a wavelength of 800 nm, compared to 1550 nm (Fig. 3.18b). This confirms the role of surface plasmon waves in enhancing the optical intensity near the Au gratings, in spite of the fact that much stronger intensity enhancement levels could be achieved at shorter optical wavelengths [51]. It should be noted that the excited surface plasmon waves are tightly confined to the Au interface. Therefore, the thin adhesion layers (e.g. Titanium) often used for facilitating Au lift-off in practical applications would have a negative impact on the discussed plasmonic enhancement.

The impulse response of the designed plasmonic photoconductor is estimated by calculating the photo-generated carrier profile and the applied bias electric field in a multi-physics finite-element solver (COMSOL). The bias voltage is set to limit the maximum induced electric field to half of the breakdown field in $In_{0.53}Ga_{0.47}As$. Figure 3.19 shows the induced electric field and the corresponding electron drift velocity inside the 60 nm-thick $In_{0.53}Ga_{0.47}As$ layer as a function of distance from the ground electrode. In spite of the rapid reduction of the induced electric field as a function of distance from the ground electrode (Fig. 3.19a), electron drift velocity exhibits a much more gradual reduction as a function of distance from the ground electrode (Fig. 3.19b). This is because the carrier drift velocity does not have a linear dependence on the applied electric field at high field intensities and saturates due to carrier scattering inside the semiconductor lattice [52–54]. As illustrated in Fig. 3.19b, electron drift velocity in $In_{0.53}Ga_{0.47}As$ remains above 0.5×10^7 cm/s while reducing the bias electric field from 100 kV/cm to 0.4 kV/cm at either side of a 20 µm long plasmonic contact electrode grating [52–54]. It should be mentioned that the drift velocity of photo-generated holes is much smaller than photo-generated electrons even at high field intensities (Fig. 3.19b). This makes electrons the dominant contributor

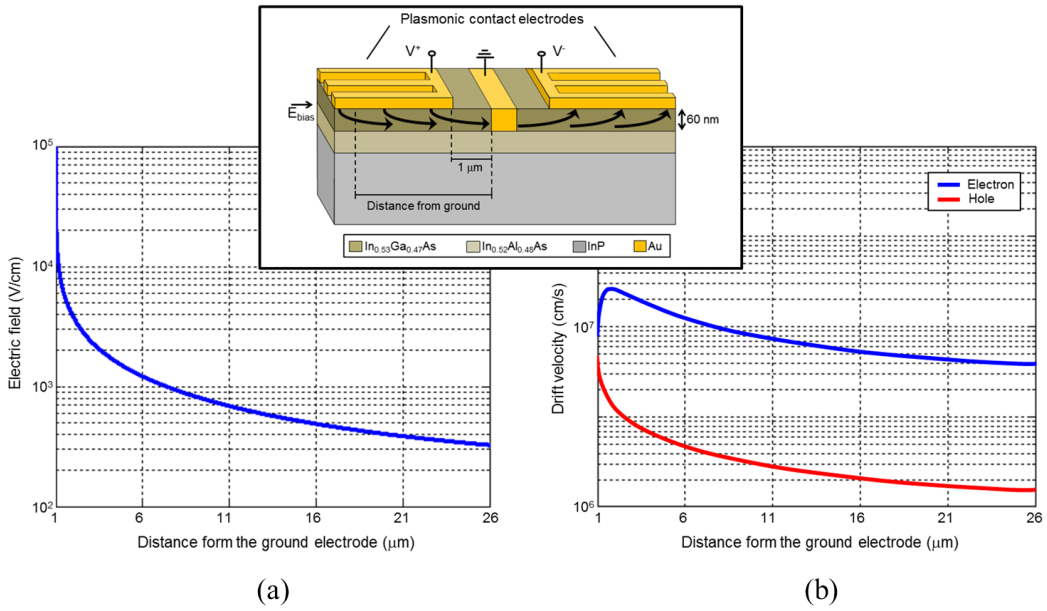

Figure 3.19: Variation of DC electric field in plasmonic terahertz emitter. (a) Induced electric field inside the $In_{0.53}Ga_{0.47}As$ layer as a function of distance from the ground electrode. The bias voltage is set to produce a maximum electric field of 10^5 V/cm (half of the $In_{0.53}Ga_{0.47}As$ breakdown field). (b) Estimated carrier drift velocity inside the $In_{0.53}Ga_{0.47}As$ layer as a function of distance from the ground electrode by using the reported carrier drift velocity in $In_{0.53}Ga_{0.47}As$ as a function of the applied electric field [52–54].

to photoconductor impulse response, similar to conventional photoconductive sources. Therefore, the nonlinear dependence of carrier drift velocity on the applied electric field allows use of relatively large photoconductor active areas with plasmonic contact electrodes without a significant reduction in the carrier drift velocity and photoconductor efficiency. The impulse response of the designed plasmonic photoconductor to a TM-polarized optical impulse is estimated by calculating the collected transient photocurrent at the contact electrodes under the influence of the induced bias electric field along a 20 µm long plasmonic contact electrode [16]. For this purpose, the photo-generated carrier density is derived from the calculated optical intensity in the $In_{0.53}Ga_{0.47}As$ active layer and combined with the electric field data in the classical drift-diffusion model to calculate the induced photocurrent.

We have analyzed the impulse response of the designed plasmonic photoconductor

at 925 nm pump wavelength in comparison with a conventional photoconductor with interdigitated Au contact electrodes (100 nm width and 2 µm pitch) fabricated on a short-carrier lifetime $In_{0.53}Ga_{0.47}As$ substrate with a carrier lifetime of 0.3 ps. The bias voltage in both cases is set to limit the maximum induced electric field to half of the breakdown field in $In_{0.53}Ga_{0.47}As$. The 925 nm pump wavelength is the highest wavelength supported by the Ti:sapphire mode-locked laser available in our lab, which is used to characterize the ultrafast response of the fabricated plasmonic photoconductive emitter prototypes. The results are presented in Fig. 3.20a, indicating the superior performance of the designed plasmonic photoconductor offering high-quantum efficiency and ultrafast operation simultaneously. The advantage of the designed plasmonic photoconductor is more apparent when comparing its responsivity with the conventional photoconductor fabricated on a short-carrier lifetime $In_{0.53}Ga_{0.47}As$ substrate. The responsivity spectra are calculated by convolving the impulse response of photoconductors with the sinusoidal power envelope of two frequency-offset optical beams as a function of optical beat frequency. The responsivity spectra (Fig. 3.20b) indicate that the designed plasmonic photoconductor offers an order of magnitude higher responsivity levels compared with the conventional photoconductor fabricated on a short-carrier lifetime $In_{0.53}Ga_{0.47}As$ substrate.

It should be mentioned that at a given pump power, the radiated power from a photoconductive terahertz emitter has a quadratic dependence on the photoconductor responsivity. Therefore, compared with the conventional photoconductors, the designed plasmonic photoconductor offers two orders of magnitude higher optical-to-terahertz conversion efficiencies. An additional advantage of the designed plasmonic photoconductor compared with conventional photoconductor designs is that the photoconductor active area along the antenna input ports can be increased without substantial increase in capacitive loading to the antenna. For example, in order to induce the same capacitive loading to terahertz radiating antenna, the photo-absorbing ac-

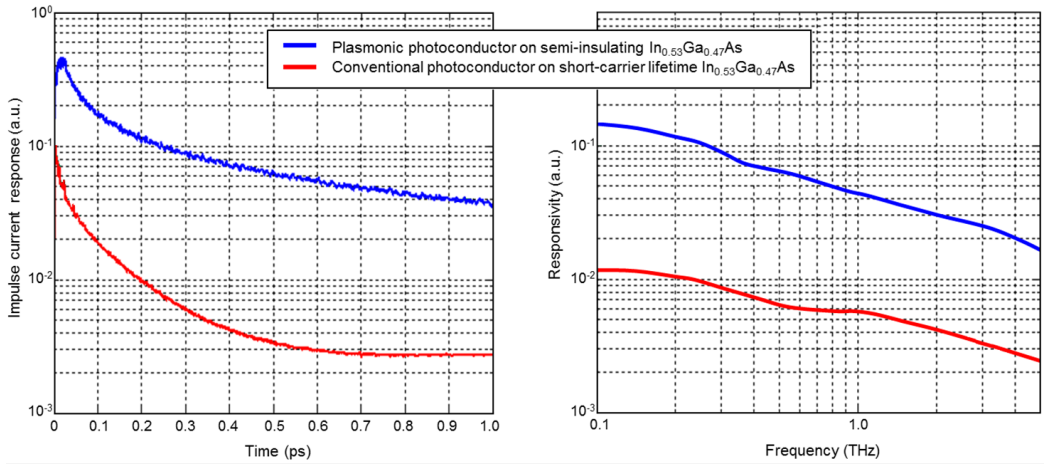

Figure 3.20: Photocarrier transport impulse response and responsivity spectrum. (a) Calculated impulse current response and (b) responsivity spectrum of the designed plasmonic photoconductor (with 200 nm pitch, 100 nm width, and 50 nm thick Au contact gratings fabricated on a 60 nm thick $In_{0.53}Ga_{0.47}As$ active layer) in comparison with a conventional photoconductor with interdigitated Au contact gratings (with 100 nm width and 2 µm pitch fabricated on a short-carrier lifetime $In_{0.53}Ga_{0.47}As$ substrate with a carrier lifetime of 0.3 ps) at 925 nm pump wavelength.

tive area of the designed plasmonic photoconductor would be 20 times larger than the active area of the discussed conventional photoconductor. This makes plasmonic photoconductive sources very attractive for operating at high pump power levels, where maximum radiated power of conventional designs is limited by the carrier screening effect and thermal breakdown.

For the first long-carrier lifetime plasmonic photoconductive terahertz emitters, the designed Au contact gratings are integrated as a part of densely spaced dipole antennas. The array of closely spaced dipole antennas is designed to increase the photoconductor active area while maintaining a small RC time-constant and high radiation resistance. We have used ADS and HFSS software packages to optimize the antenna array structure for maximum radiation power, by combining the antenna radiation parameters, photoconductor parasitics, and the amount of injected current based on photoconductor active area [13]. Arrays of 2-10 µm wide dipole antennas

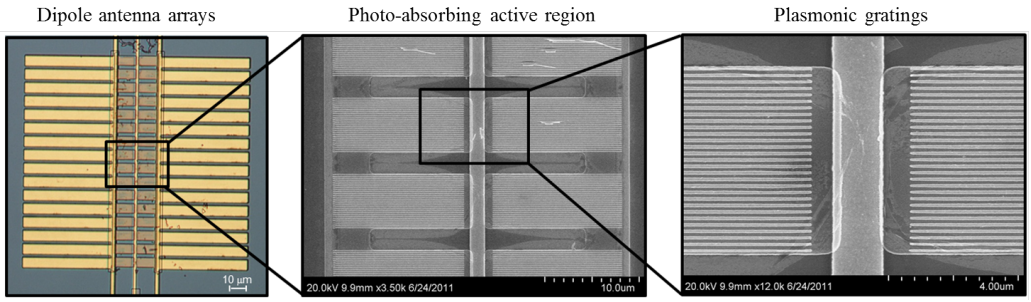

Figure 3.21: Images of a plasmonic photoconductive terahertz emitter prototype based on nanoscale Au contact electrode gratings and 6 µm wide, 130 µm long dipole antenna arrays.

with lengths varying between 130-260 µm and separated laterally by 2 µm are selected for the prototype devices.

3.3.2 Methods

3.3.2.1 Fabrication

Following our analytical modeling, plasmonic photoconductive emitter prototypes were fabricated on a 60 nm thick undoped $In_{0.53}Ga_{0.47}As$ layer, epitaxially-grown on a lattice-matched un-doped $In_{0.52}Al_{0.48}As$ buffer layer on a semi-insulating InP substrate (Fig. 3.21). The undoped $In_{0.53}Ga_{0.47}As$ and $In_{0.52}Al_{0.48}As$ layers together with the 500 µm thick semi-insulating InP substrate would introduce a negligible absorption loss at terahertz frequencies. Nanoscale contact gratings were patterned using electron-beam lithography followed by Ti/Au (3 nm/50 nm) deposition and lift-off. The $In_{0.53}Ga_{0.47}As$ layer is etched away from the regions outside the photoconductor active area to reduce the background photocurrent that does not contribute to terahertz radiation. Dipole antenna arrays are patterned using optical lithography on a 150 nm thick SiO_2 layer deposited on $In_{0.53}Ga_{0.47}As$ to reduce antenna losses on the low-resistivity $In_{0.53}Ga_{0.47}As$ substrate. Complete fabrication details are listed in Appendix C.

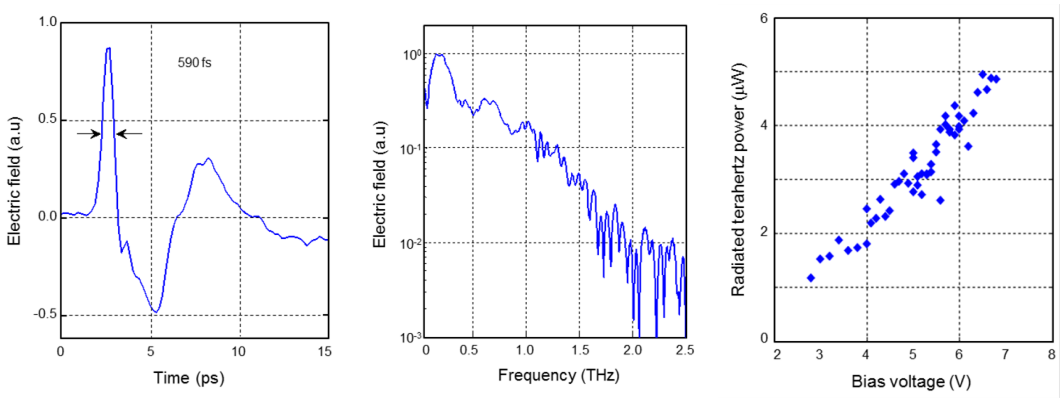

(a) (b) (c)

Figure 3.22: Measure radiation from a fabricated plasmonic photoconductive terahertz emitter prototype with a dipole antenna length of 260 µm. The (a) time-domain and (b) frequency-domain radiated field. (c) The measured radiated power under an optical pump illumination of 85 mW and as a function of the bias voltage.

3.3.3 Experimental Results

The ultrafast operation of the plasmonic photoconductive emitter prototypes is confirmed by characterizing their radiation in a time-domain spectroscopy setup pumped by a mode-locked Ti:sapphire laser providing 200 fs pump pulses at 925 nm center wavelength with a 76 MHz repetition rate. An electro-optic sampling detection scheme using a ZnTe crystal is used to detect the radiated electric field. Figure 3.22a shows the measured time-domain radiation of a plasmonic photoconductive emitter prototype with an antenna length of 260 µm. A 590 fs FWHM is measured in the time domain, showing the ultrafast response of the device without using a short-carrier lifetime semiconductor. The 590 fs wide radiation peak is followed by the resonant response of the 260 µm long dipole antenna. Figure 3.22b shows the corresponding frequency-domain radiation from the plasmonic photoconductive emitter prototype, indicating a terahertz radiation bandwidth of more than 1.5 THz. The radiation peak at 0.25 THz is associated with the resonance peak of the dipole antenna of the characterized prototype.

Radiated power from the plasmonic photoconductive emitter prototypes are mea-

sured by using a pyroelectric detector (Spectrum Detector, Inc. SPI-A-65 THz). A 5 Hz modulation required by the pyroelectric detector was provided by an optical chopper in the optical pump path. The modulated radiation was measured with a lock-in amplifier and converted to terahertz power by using the pyroelectric detector responsivity in the 0.1-2 THz frequency range. Figure 3.22c shows the measured radiated power from a plasmonic photoconductive emitter prototype with antenna length of 260 µm, under an optical pump illumination of 85 mW and as a function of the bias voltage.

3.3.4 Discussion

The linear dependence of the radiated terahertz power and bias voltage indicates the insufficient induced electric field for efficient acceleration of the photo-generated carriers. This limitation is associated with the low bandgap energy of InGaAs, leading to high dark current levels. Under this constraint, a radiated power of 5 µW is measured for the plasmonic photoconductive terahertz emitter prototype at a bias voltage of 6.5 V. It should be mentioned that the high dark current associated with the low bandgap energy of InGaAs has been the major obstacle for InGaAs-based photoconductive emitters. There have been extensive studies on various techniques to mitigate this challenge [55–57] and very promising solutions have been offered for reducing photoconductor dark current by embedding InGaAs between InAlAs trapping layers [58, 59]. Although the output power of the presented plasmonic photoconductive terahertz emitter can be further enhanced using high resistivity photo-absorbing substrates, its maximum output power in the absence of such high resistivity photo-absorbing substrates is fifty times higher than previously demonstrated photoconductive emitters with planar dipole antennas fabricated on high resistivity InGaAs/InAlAs photo-absorbing layers [58].

In summary, a photoconductive terahertz emitter based on plasmonic contact

electrodes on a high-quality crystalline substrate is presented for the first time and characterized experimentally. The nanoscale carrier transport path lengths provided by plasmonic contact electrode gratings allow high quantum efficiency and ultrafast operation simultaneously. It also eliminates the need to use short-carrier lifetime substrates which are a major source of quantum efficiency degradation in conventional photoconductors. Additionally, the photo-absorbing active area of plasmonic photoconductive terahertz emitters can be increased without a significant increase in the capacitive loading to the terahertz radiating antenna. This allows high quantum-efficiency operation at high pump power levels by preventing the carrier screening effect and thermal breakdown. The presented plasmonic photoconductive terahertz emitter would benefit from high-aspect ratio nanoscale contact electrodes embedded inside the substrate [49, 60], which enable a significant increase in optical-to-terahertz conversion efficiency by ultrafast collection of photo-generated carriers in deeper substrate regions.

References

[1] T. W. Ebbesen, H. J. Lezec, H. F. Ghaemi, T. Thio, and P. A. Wolff, "Extraordinary optical transmission through sub-wavelength hole arrays", *Nature*, vol. 391, no. 6668, pp. 667–669, 1998.

[2] J. Bravo-Abad, A. Degiron, F. Przybilla, C. Genet, F. J. García-Vidal, L. Martín-Moreno, and T. W. Ebbesen, "How light emerges from an illuminated array of subwavelength holes", *Nature Physics*, vol. 2, no. 2, pp. 120–123, Jan. 2006.

[3] J. Zhang and L. Zhang, "Nanostructures for surface plasmons", *Advances in Optics and Photonics*, vol. 4, no. 2, pp. 157, July 2012.

[4] A. P. Hibbins, B. R. Evans, and J. R. Sambles, "Experimental Verification of Designer Surface Plasmons", *Science*, vol. 308, no. 5722, pp. 670–672, Apr. 2005.

[5] C. Genet and T. W. Ebbesen, "Light in tiny holes.", *Nature*, vol. 445, no. 7123, pp. 39–46, Jan. 2007.

[6] A. Degiron and T. W. Ebbesen, "The role of localized surface plasmon modes

in the enhanced transmission of periodic subwavelength apertures", *Journal of Optics-A-Pure and Applied Optics*, vol. 7, no. 2, pp. 90, 2005.

[7] W. L. Barnes, A. Dereux, and T. W. Ebbesen, "Surface plasmon subwavelength optics", *Nature*, vol. 424, no. 6950, pp. 824–830, 2003.

[8] K. Lee and Q.-H. Park, "Coupling of Surface Plasmon Polaritons and Light in Metallic Nanoslits", *Physical Review Letters*, vol. 95, no. 10, pp. 103902, Sept. 2005.

[9] A. Barbara, P. Quémerais, E. Bustarret, and T. Lopez-Rios, "Optical transmission through subwavelength metallic gratings", *Physical Review B*, vol. 66, no. 16, Oct. 2002.

[10] J. Porto, F. J. García-Vidal, and J. Pendry, "Transmission Resonances on Metallic Gratings with Very Narrow Slits", *Physical Review Letters*, vol. 83, no. 14, pp. 2845–2848, Oct. 1999.

[11] P. C. Upadhya, W. Fan, A. Burnett, J. Cunningham, A. G. Davies, E. H. Linfield, J. Lloyd-Hughes, E. Castro-Camus, M. B. Johnston, and H. E. Beere, "Excitation-density-dependent generation of broadband terahertz radiation in an asymmetrically excited photoconductive antenna", *Optics Letters*, vol. 32, no. 16, pp. 2297, Aug. 2007.

[12] S. E. Ralph and D. R. Grischkowsky, "Trap-enhanced electric fields in semi-insulators: The role of electrical and optical carrier injection", *Applied Physics Letters*, vol. 59, no. 16, pp. 1972, Oct. 1991.

[13] C. W. Berry and M. Jarrahi, "Principles of Impedance Matching in Photoconductive Antennas", *Journal of Infrared, Millimeter, and Terahertz Waves*, pp. 1–8, Sept. 2012.

[14] J. Požela and A. Reklaitis, "Electron transport properties in GaAs at high electric fields", *Solid-State Electronics*, vol. 23, no. 9, pp. 927–933, Sept. 1980.

[15] C. W. Berry and M. Jarrahi, "Plasmonically-Enhanced Localization of Light into Photoconductive Antennas - OSA Technical Digest (CD)", in *Conference on Lasers and Electro-Optics*. May 2010, p. CFI2, Optical Society of America.

[16] C. W. Berry and M. Jarrahi, "Ultrafast photoconductors based on plasmonic gratings", in *2011 International Conference on Infrared, Millimeter, and Terahertz Waves*. Oct. 2011, pp. 1–2, IEEE.

[17] J. Lloyd-Hughes, S. K. E. Merchant, L. Fu, H. H. Tan, C. Jagadish, E. Castro-Camus, and M. B. Johnston, "Influence of surface passivation on ultrafast carrier dynamics and terahertz radiation generation in GaAs", *Applied Physics Letters*, vol. 89, no. 23, pp. 232102, Dec. 2006.

[18] C. Headley, L. Fu, P. Parkinson, X. Xu, J. Lloyd-Hughes, C. Jagadish, and M. B. Johnston, "Improved Performance of GaAs-Based Terahertz Emitters via Surface Passivation and Silicon Nitride Encapsulation", *IEEE Journal of Selected Topics in Quantum Electronics*, vol. 17, no. 1, pp. 17–21, Jan. 2011.

[19] P. G. Huggard, C. J. Shaw, J. A. Cluff, and S. R. Andrews, "Polarization-dependent efficiency of photoconducting THz transmitters and receivers", *Applied Physics Letters*, vol. 72, no. 17, pp. 2069, Apr. 1998.

[20] W. Shi, L. Hou, and X. Wang, "High effective terahertz radiation from semi-insulating-GaAs photoconductive antennas with ohmic contact electrodes", *Journal of Applied Physics*, vol. 110, no. 2, pp. 023111, July 2011.

[21] Q. Wu and X.-C. Zhang, "Free-space electro-optics sampling of mid-infrared pulses", *Applied Physics Letters*, vol. 71, no. 10, pp. 1285, Sept. 1997.

[22] Y. Cai, I. Brener, J. Lopata, J. Wynn, L. Pfeiffer, J. B. Stark, Q. Wu, X. C. Zhang, and J. F. Federici, "Coherent terahertz radiation detection: Direct comparison between free-space electro-optic sampling and antenna detection", *Applied Physics Letters*, vol. 73, no. 4, pp. 444, July 1998.

[23] C. W. Berry, N. Wang, M. R. Hashemi, M. Unlu, and M. Jarrahi, "Significant performance enhancement in photoconductive terahertz optoelectronics by incorporating plasmonic contact electrodes", *Nature Communications*, vol. 4, pp. 1622, 2013.

[24] C. W. Berry and M. Jarrahi, "Terahertz generation using plasmonic photoconductive gratings", *New Journal of Physics*, vol. 14, no. 10, pp. 105029, Oct. 2012.

[25] W. L. Stutzman and G. A. Thiele, *Antenna Theory and Design*, John Wiley & Sons, second edition, 1998.

[26] J. A. Schuller, E. S. Barnard, W. Cai, Y. C. Jun, J. S. White, and M. L. Brongersma, "Plasmonics for extreme light concentration and manipulation.", *Nature materials*, vol. 9, no. 3, pp. 193–204, Mar. 2010.

[27] A. Hartschuh, E. J. Sánchez, X. S. Xie, and L. Novotny, "High-resolution near-field Raman microscopy of single-walled carbon nanotubes.", *Physical review letters*, vol. 90, no. 9, pp. 095503, Mar. 2003.

[28] H. Frey, S. Witt, K. Felderer, and R. Guckenberger, "High-Resolution Imaging of Single Fluorescent Molecules with the Optical Near-Field of a Metal Tip", *Physical Review Letters*, vol. 93, no. 20, pp. 200801–, Nov. 2004.

[29] E. Cubukcu, E. A. Kort, K. B. Crozier, and F. Capasso, "Plasmonic laser antenna", *Applied Physics Letters*, vol. 89, no. 9, pp. 093120, Aug. 2006.

[30] N. Yu, J. Fan, Q. J. Wang, C. Pflügl, L. Diehl, T. Edamura, M. Yamanishi, H. Kan, and F. Capasso, "Small-divergence semiconductor lasers by plasmonic collimation", *Nature Photonics*, vol. 2, no. 9, pp. 564–570, July 2008.

[31] H. A. Atwater and A. Polman, "Plasmonics for improved photovoltaic devices.", *Nature materials*, vol. 9, no. 3, pp. 205–13, Mar. 2010.

[32] R. A. Pala, J. White, E. S. Barnard, J. Liu, and M. L. Brongersma, "Design of Plasmonic Thin-Film Solar Cells with Broadband Absorption Enhancements", *Advanced Materials*, vol. 21, no. 34, pp. 3504–3509, Sept. 2009.

[33] T. Ishi, J. Fujikata, K. Makita, T. Baba, and K. Ohashi, "Si Nano-Photodiode with a Surface Plasmon Antenna", *Japanese Journal of Applied Physics*, vol. 44, no. 12, pp. L364–L366, Mar. 2005.

[34] L. Tang, S. E. Kocabas, S. Latif, A. K. Okyay, D.-S. Ly-Gagnon, K. C. Saraswat, and D. A. B. Miller, "Nanometre-scale germanium photodetector enhanced by a near-infrared dipole antenna", *Nature Photonics*, vol. 2, no. 4, pp. 226–229, Mar. 2008.

[35] J. Dintinger, I. Robel, P. V. Kamat, C. Genet, and T. W. Ebbesen, "Terahertz All-Optical Molecule- Plasmon Modulation", *Advanced Materials*, vol. 18, no. 13, pp. 1645–1648, July 2006.

[36] C. W. Berry, J. Moore, and M. Jarrahi, "Design of reconfigurable metallic slits for terahertz beam modulation", *Optics Express*, vol. 19, no. 2, pp. 1236, Jan. 2011.

[37] S.-G. Park, K. H. Jin, M. Yi, J. C. Ye, J. Ahn, and K.-H. Jeong, "Enhancement of terahertz pulse emission by optical nanoantenna", *ACS nano*, vol. 6, no. 3, pp. 2026–2031, Mar. 2012.

[38] M. Beck, H. Schäfer, G. Klatt, J. Demsar, S. Winnerl, M. Helm, and T. Dekorsy, "Impulsive terahertz radiation with high electric fields from an amplifier-driven large-area photoconductive antenna", *Optics Express*, vol. 18, no. 9, pp. 9251, Apr. 2010.

[39] M. Jarrahi and T. H. Lee, "High-power tunable terahertz generation based on photoconductive antenna arrays", in *2008 IEEE MTT-S International Microwave Symposium Digest*. June 2008, pp. 391–394, IEEE.

[40] M. Jarrahi, "Terahertz Radiation-Band Engineering Through Spatial Beam-Shaping", *IEEE Photonics Technology Letters*, vol. 21, no. 13, pp. 830–832, July 2009.

[41] T. Hattori, K. Egawa, S.-i. Ookuma, and T. Itatani, "Intense Terahertz Pulses from Large-Aperture Antenna with Interdigitated Electrodes", *Japanese Journal of Applied Physics*, vol. 45, no. No. 15, pp. L422–L424, Apr. 2006.

[42] J. H. Kim, A. Polley, and S. E. Ralph, "Efficient photoconductive terahertz source using line excitation", *Optics Letters*, vol. 30, no. 18, pp. 2490, Sept. 2005.

[43] A. Dreyhaupt, S. Winnerl, T. Dekorsy, and M. Helm, "High-intensity terahertz radiation from a microstructured large-area photoconductor", *Applied Physics Letters*, vol. 86, no. 12, pp. 121114, Mar. 2005.

[44] G. C. Loata, M. D. Thomson, T. Loffler, and H. G. Roskos, "Radiation field screening in photoconductive antennae studied via pulsed terahertz emission spectroscopy", *Applied Physics Letters*, vol. 91, no. 23, pp. 232506, Dec. 2007.

[45] M. B. Gray, D. A. Shaddock, C. C. Harb, and H.-A. Bachor, "Photodetector designs for low-noise, broadband, and high-power applications", *Review of Scientific Instruments*, vol. 69, no. 11, pp. 3755, Nov. 1998.

[46] A. W. Jackson, J. P. Ibbetson, A. C. Gossard, and U. K. Mishra, "Reduced thermal conductivity in low-temperature-grown GaAs", *Applied Physics Letters*, vol. 74, no. 16, pp. 2325, Apr. 1999.

[47] E. R. Brown, A. W. M. Lee, B. S. Navi, and J. E. Bjarnason, "Characterization of a planar self-complementary square-spiral antenna in the THz region", *Microwave and Optical Technology Letters*, vol. 48, no. 3, pp. 524–529, Mar. 2006.

[48] Y. Huo, G. W. Taylor, and R. Bansal, "Planar Log-Periodic Antennas on Extended Hemishperical Silicon Lenses for Millimeter/Submillimeter Wave Detection Applications", *International Journal of Infrared and Millimeter Waves*, vol. 23, no. 6, pp. 819–839, 2002.

[49] B.-Y. Hsieh and M. Jarrahi, "Analysis of periodic metallic nano-slits for efficient interaction of terahertz and optical waves at nano-scale dimensions", *Journal of Applied Physics*, vol. 109, no. 8, pp. 084326, Apr. 2011.

[50] B.-Y. Hsieh, N. Wang, and M. Jarrahi, "Toward Ultrafast Pump-Probe Measurements at the Nanoscale", *Optics and Photonics News*, vol. 22, no. 12, pp. 48, Dec. 2011.

[51] M. Staffaroni, J. Conway, S. Vedantam, J. Tang, and E. Yablonovitch, "Circuit analysis in metal-optics", *Photonics and Nanostructures - Fundamentals and Applications*, vol. 10, no. 1, pp. 166–176, Jan. 2012.

[52] V. Balynas, A. Krotkus, A. Stalnionis, A. T. Gorelionok, N. M. Shmidt, and J. A. Tellefsen, "Time-resolved, hot-electron conductivity measurement using an electro-optic sampling technique", *Applied Physics A Solids and Surfaces*, vol. 51, no. 4, pp. 357–360, Oct. 1990.

[53] S. R. Ahmed, B. R. Nag, and M. D. Roy, "Hot-electron transport in In0.53Ga0.47As", *Solid-State Electronics*, vol. 28, no. 12, pp. 1193–1197, Dec. 1985.

[54] S. Adachi, *Physical Properties of III-V Semiconductor Compounds: InP, InAs, GaAs, GaP, InGaAs, and InGaAsP*, vol. 1992, John Wiley & Sons, 1992.

[55] J. Mangeney, N. Chimot, L. Meignien, N. Zerounian, P. Crozat, K. Blary, J. F. Lampin, and P. Mounaix, "Emission characteristics of ion-irradiated In_0.53Ga_0.47As based photoconductive antennas excited at 1.55 m", *Optics Express*, vol. 15, no. 14, pp. 8943, July 2007.

[56] C. Carmody, H. H. Tan, C. Jagadish, A. Gaarder, and S. Marcinkevicius, "Ion-implanted In[sub 0.53]Ga[sub 0.47]As for ultrafast optoelectronic applications", *Applied Physics Letters*, vol. 82, no. 22, pp. 3913, June 2003.

[57] M. Suzuki and M. Tonouchi, "Fe-implanted InGaAs terahertz emitters for 1.56μm wavelength excitation", *Applied Physics Letters*, vol. 86, no. 5, pp. 051104, Jan. 2005.

[58] H. Roehle, R. J. B. Dietz, H. J. Hensel, J. Böttcher, H. Künzel, D. Stanze, M. Schell, and B. Sartorius, "Next generation 15 m terahertz antennas: mesa-structuring of InGaAs/InAlAs photoconductive layers", *Optics Express*, vol. 18, no. 3, pp. 2296, Jan. 2010.

[59] B. Sartorius, H. Roehle, H. Künzel, J. Böttcher, M. Schlak, D. Stanze, H. Venghaus, and M. Schell, "All-fiber terahertz time-domain spectrometer operating at 1.5 μm telecom wavelengths", *Optics Express*, vol. 16, no. 13, pp. 9565, June 2008.

[60] B.-Y. Hsieh and M. Jarrahi, "Simultaneous focusing of terahertz and optical waves into nano-scale", in *2011 International Conference on Infrared, Millimeter, and Terahertz Waves*. Oct. 2011, pp. 1–2, IEEE.

CHAPTER IV

Conclusion

In this work a new architecture for photoconductive terahertz sources is presented. By incorporating plasmonic contact electrodes into the active region of the photoconductor, efficient optical transmission is obtained into the nanoscale regions next to the contact electrodes. This reduces the distance that the average photocarrier must travel in the substrate from the microns to tens of nanometers, which significantly increases the amount of electrical current that can drive the terahertz antenna in a sub-picosecond timescale. We experimentally show that incorporating this design can offer up to 50 times higher radiated power and optical-to-terahertz conversion efficiency than similar, conventional designs. We show that the plasmonic electrode based photoconductive terahertz source architecture can be integrated with a variety of terahertz antennas including a broadband, logarithmic spiral antenna. Using a two dimensional array of plasmonic electrode based photoconductive terahertz sources, we experimentally demonstrate up to 1.9 mW of terahertz radiation. Following this demonstration, even higher power sources can be implemented by simply increasing the size of the antenna array. Finally, using plasmonic electrodes, we show that we can create a photoconductor with an ultrafast response time without the use of a short-carrier lifetime substrate. This opens the possibility of using a variety of high performance substrates such as GaN, which offers a very high thermal conductivity, saturation velocity, and breakdown field, and graphene, which offers very high carrier mobilities.

APPENDICES

APPENDIX A

Fabrication of Plasmonic Electrode Based Bowtie Antennas on LT-GaAs

1. Fabricate plasmonic gratings (Fig. A.1a)
   (a) Clean the semiconductor wafer by immersing in acetone (2 min) followed by isopropanol (2 min), and rinsing with deionized water (10 sec).
   (b) Dry the sample with nitrogen, and heat it on a hotplate at 115 °C for 90 sec to remove any remaining water.
   (c) Spin MicroChem 950K PMMA A4 on the sample at 4,000 rpm for 45 sec. Pre-bake the resist on a hotplate at 180 °C for 3 min.
   (d) Load the sample into an electron beam lithography tool (JEOL JBX-6300-FS). Expose the plasmonic grating pattern at a base dose around 650 μC/cm^2, using a 100 kV acceleration voltage.
   (e) Develop PMMA by immersing the sample in a MIBK:IPA 1:3 mixture for 60 sec. Immediately transfer the sample to a solution of pure isopropanol for 60 sec.
   (f) Rinse the sample with deionized water for 10 sec and then dry the sample with nitrogen.
   (g) Load the sample into a plasma stripper (YES-CV200RFS). Descum the sample using 30 W RF power at 30 °C with a 100 sccm O_2 flow rate for 10 sec.
   (h) Remove surface oxide by immersing in a HCl:H_2O 3:10 mixture for 30 sec. Immediately transfer the sample to a cascade rinse of deionized water for 4 min.

(i) Transfer the sample to a beaker of deionized water to minimize exposure to atmospheric oxygen before metal deposition.

(j) Take beaker containing the sample in deionized water to a metal evaporator (Denton SJ-20). Vent the chamber and then remove, dry, and load the sample into the chamber (these steps should be followed without interruption to prevent surface oxide formation on the sample).

(k) Pump the chamber to a pressure below 2×10^{-6} Torr. Deposit Ti/Au (50/450 Å).

(l) Vent the chamber and remove the sample.

(m) In order to lift-off the deposited metal, place the sample on a Teflon holder in a beaker of acetone, cover, and leave overnight. Uncover the beaker, place it in an ultrasonic agitator, and wait until all unwanted metal is removed (typically 30 sec).

2. Deposit SiO2 passivation (Fig. A.1b)

(a) Clean the sample as in Steps 1.a - 1.b.

(b) Load the sample in a plasma-enhanced chemical vapor deposition tool (GSI PECVD). Deposit 1500 Å of SiO_2 at 200 °C.

3. Open contact vias through SiO_2 (Fig. A.1c)

(a) Clean the sample as in Steps 1.a - 1.b.

(b) Spin on HMDS at 4,000 rpm for 30 sec. Spin on Megaposit SPR 220-3.0 photoresist at 4,000 rpm for 30 sec. Pre-bake the resist on a hotplate at 115 °C for 90 sec.

(c) Load the sample and mask plate into projection lithography stepper (GCA AutoStep 200). Align the sample and expose.

(d) Post-bake the exposed photoresist on a hotplate at 115 °C for 90 sec.

(e) Develop resist in AZ 300 MIF developer for 60 sec.

(f) Immediately move the sample to a cascade rinse of deionized water for 4 min. Dry the sample with nitrogen.

(g) Load the sample into a reactive ion etcher (LAM 9400). Etch SiO_2 using a TCP RF power of 500 W, a Bias RF power of 100 W, 15 sccm of SF_6, 50 sccm of C_4F_8, 50 sccm He, 50 sccm of Ar for 80 sec.

(h) Remove the bulk of the photoresist by placing the sample in acetone (5 min) followed by isopropanol (2 min). Rinse in deionized water (10 sec). Dry with nitrogen.

(i) Remove the residual photoresist by loading the sample in a plasma stripper (YES-CV200RFS). Remove the photoresist using 800 W RF power at 30 °C with a 100 sccm O_2 flow rate for 5 min.

4. Fabricate antennas and bias lines (Fig. A.1d)

   (a) Repeat Steps 3.a - 3.f to pattern antennas and bias lines.

   (b) Repeat Steps 1.h - 1.i to remove surface oxide.

   (c) Take the beaker containing the sample and deionized water to a metal evaporator (Denton SJ-20).

   (d) Vent the chamber and then quickly remove, dry, and load the sample into the chamber.

   (e) Pump the chamber to a pressure below 2×10^{-6} Torr. Deposit Ti/Au (100/4,000 Å).

   (f) Vent the chamber and remove the sample.

   (g) Repeat Step 1.m to lift-off the deposited metal.

5. Package the sample

   (a) Glue the edges of a 12 mm diameter hyper-hemispherical silicon lens to a 2 inch aluminum washer with 8 mm hole.

   (b) Glue a PCB board with metal traces, to which one can easily solder, to the aluminum washer.

   (c) Mount the fabricated plasmonic photoconductive terahertz emitter prototypes on the silicon lens using thin epoxy.

   (d) Wire bond the device contact pads to a PCB board glued on the same aluminum washer.

   (e) Solder wires to the metal traces on the PCB board.

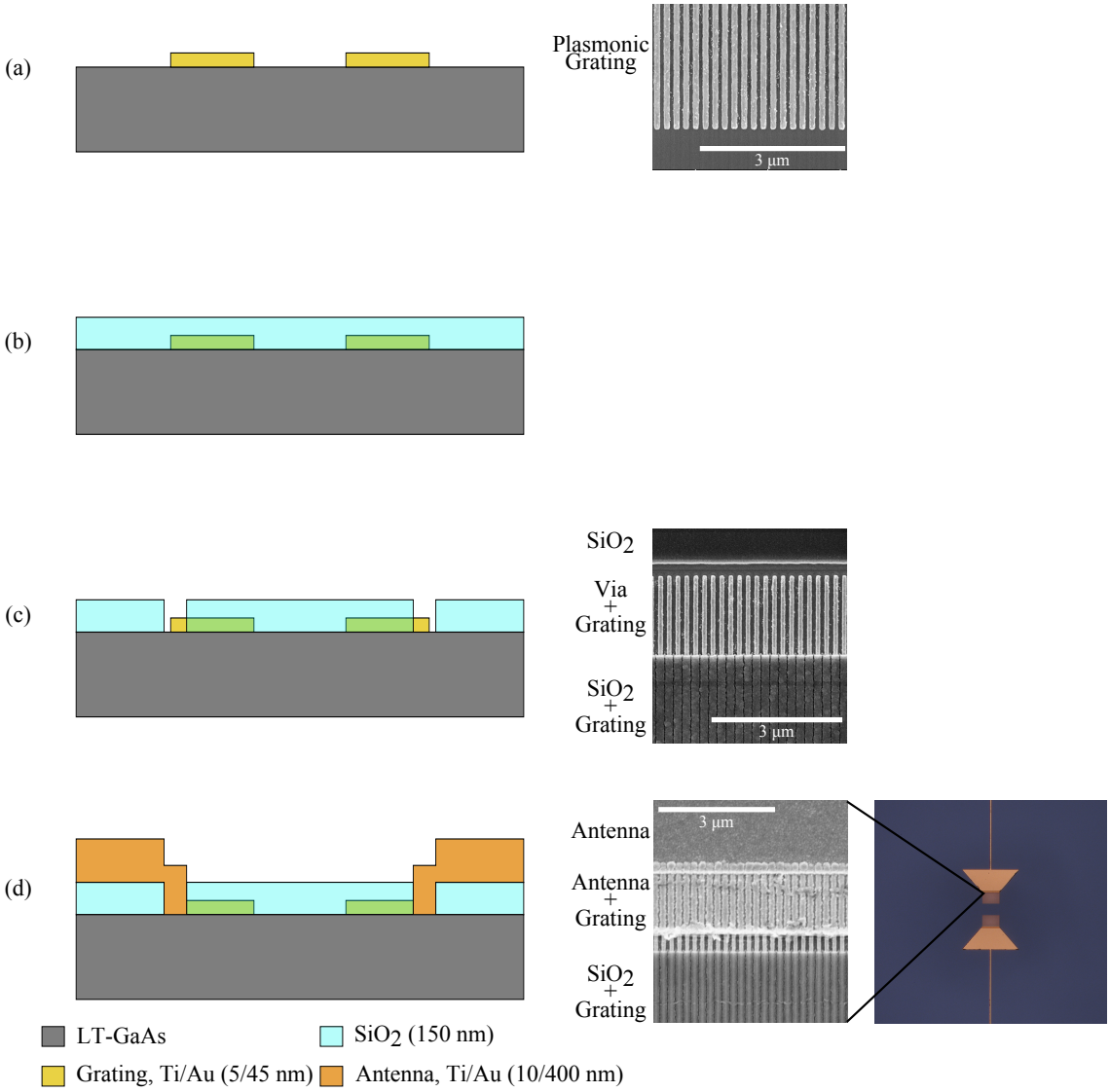

Figure A.1: Fabrication process of bowtie emitter. Left: Process flow. Right: SEM and microscope images. (a) Plasmonic gratings are patterned through direct-write electron beam lithography followed by deposition and liftoff of Ti/Au (5/45 nm). (b) 150 nm of PECVD SiO_2 is deposited. (c) Contact openings are etched in SiO_2 via plasma etching. (d) Antennas and contact pads are formed through deposition and liftoff of Ti/Au (10/400 nm).

APPENDIX B

Fabrication of Plasmonic Electrode Based Logarithmic Spiral Antennas on LT-GaAs

1. Fabricate plasmonic gratings (Fig. B.1a)

   (a) Clean the semiconductor wafer by immersing in acetone (2 min) followed by isopropanol (2 min), and rinsing with deionized water (10 sec).

   (b) Dry the sample with nitrogen and heat it on a hotplate at 115 °C for 90 sec to remove any remaining water.

   (c) Spin MicroChem 950K PMMA A4 on the sample at 4,000 rpm for 45 sec. Pre-bake the resist on a hotplate at 180 °C for 3 min.

   (d) Load the sample into an electron beam lithography tool (JEOL JBX-6300-FS). Expose the plasmonic grating pattern at a base dose around 650 μC/cm^2, using a 100 kV acceleration voltage.

   (e) Develop PMMA by immersing the sample in a MIBK:IPA 1:3 mixture for 60 sec. Immediately transfer the sample to a solution of pure isopropanol for 60 sec.

   (f) Rinse the sample with deionized water for 10 sec and then dry the sample with nitrogen.

   (g) Load the sample into a plasma stripper (YES-CV200RFS). Descum the sample using 30 W RF power at 30 °C with a 100 sccm O_2 flow rate for 10 sec.

   (h) Remove surface oxide by immersing in a HCl:H_2O 3:10 mixture for 30 sec. Immediately transfer the sample to a cascade rinse of deionized water for 4 min.

   (i) Transfer the sample to a beaker of deionized water to minimize exposure to atmospheric oxygen before metal deposition.

(j) Take beaker containing the sample in deionized water to a metal evaporator (Denton SJ-20). Vent the chamber and then remove, dry, and load the sample into the chamber (these steps should be followed without interruption to prevent surface oxide formation on the sample).

(k) Pump the chamber to a pressure below 2×10^{-6} Torr. Deposit Ti/Au (50/450 Å).

(l) Vent the chamber and remove the sample.

(m) In order to lift-off the deposited metal, place the sample on a Teflon holder in a beaker of acetone, cover, and leave overnight. Uncover the beaker, place it in an ultrasonic agitator, and wait until all unwanted metal is removed (typically 30 sec).

2. Deposit SiO2 passivation (Fig. B.1b)

(a) Clean the sample as in Steps 1.a - 1.b.

(b) Load the sample in a plasma-enhanced chemical vapor deposition tool (GSI PECVD). Deposit 1500 Å of SiO_2 at 200 °C.

3. Open contact vias through SiO_2 (Fig. B.1c)

(a) Clean the sample as in Steps 1.a - 1.b.

(b) Spin on HMDS at 4,000 rpm for 30 sec. Spin on Megaposit SPR 220-3.0 photoresist at 4,000 rpm for 30 sec. Pre-bake the resist on a hotplate at 115 °C for 90 sec.

(c) Load the sample and mask plate into projection lithography stepper (GCA AutoStep 200). Align the sample and expose.

(d) Post-bake the exposed photoresist on a hotplate at 115 °C for 90 sec.

(e) Develop resist in AZ 300 MIF developer for 60 sec.

(f) Immediately move the sample to a cascade rinse of deionized water for 4 min. Dry the sample with nitrogen.

(g) Load the sample into a reactive ion etcher (LAM 9400). Etch SiO_2 using a TCP RF power of 500 W, a Bias RF power of 100 W, 15 sccm of SF_6, 50 sccm of C_4F_8, 50 sccm He, 50 sccm of Ar for 80 sec.

(h) Remove the bulk of the photoresist by placing the sample in acetone (5 min) followed by isopropanol (2 min). Rinse in deionized water (10 sec). Dry with nitrogen.

(i) Remove the residual photoresist by loading the sample in a plasma stripper (YES-CV200RFS). Remove the photoresist using 800 W RF power at 30 °C with a 100 sccm O_2 flow rate for 5 min.

4. Fabricate antennas and bias lines (Fig. B.1d)

(a) Repeat Steps 3.a - 3.f to pattern antennas and bias lines.

(b) Repeat Steps 1.h - 1.i to remove surface oxide.

(c) Take the beaker containing the sample and deionized water to a metal evaporator (Denton SJ-20).

(d) Vent the chamber and then quickly remove, dry, and load the sample into the chamber.

(e) Pump the chamber to a pressure below 2×10^{-6} Torr. Deposit Ti/Au (100/4,000 Å).

(f) Vent the chamber and remove the sample.

(g) Repeat Step 1.m to lift-off the deposited metal.

5. Package the sample

(a) Glue the edges of a 12 mm diameter hyper-hemispherical silicon lens to a 2 inch aluminum washer with 8 mm hole.

(b) Glue a PCB board with metal traces, to which one can easily solder, to the aluminum washer.

(c) Mount the fabricated plasmonic photoconductive terahertz emitter prototypes on the silicon lens using thin epoxy.

(d) Wire bond the device contact pads to a PCB board glued on the same aluminum washer.

(e) Solder wires to the metal traces on the PCB board.

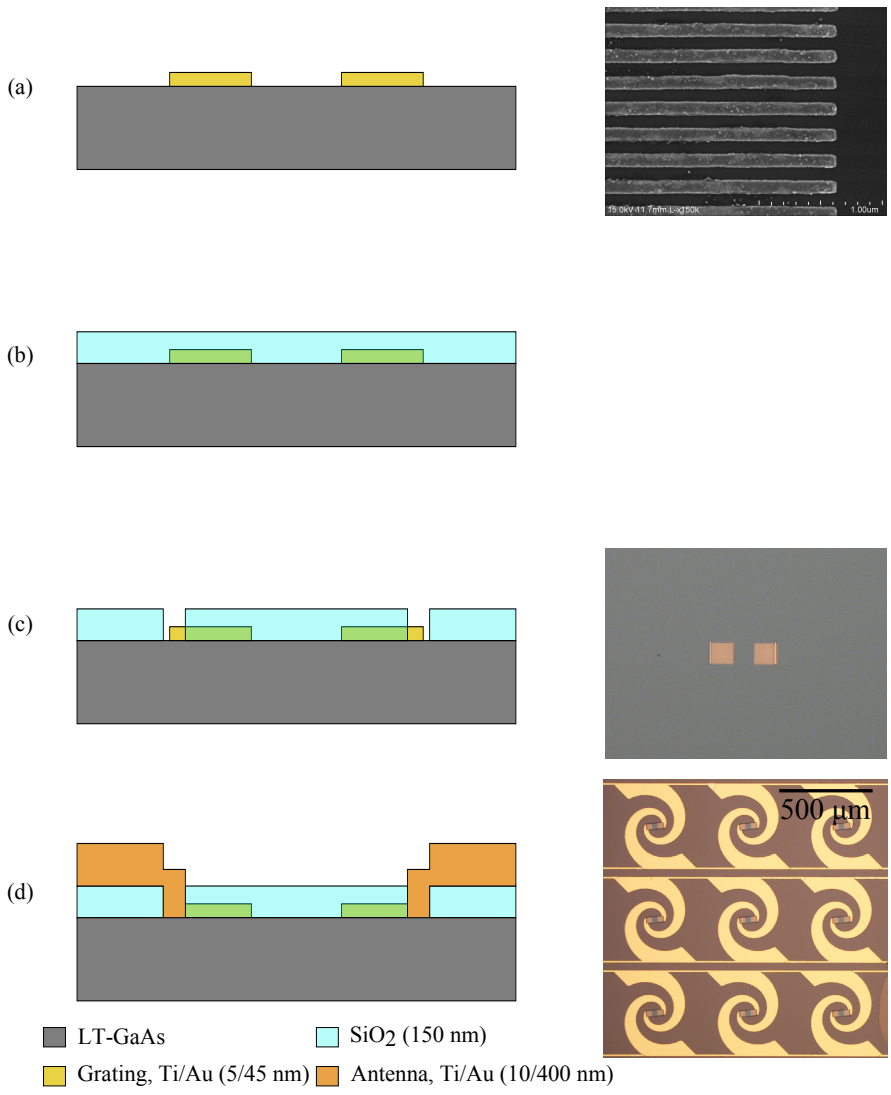

Figure B.1: Fabrication process of emitter array. Left: Process flow. Right: SEM and microscope images. (a) Plasmonic gratings are patterned through direct-write electron beam lithography followed by deposition and liftoff of Ti/Au (5/45 nm). (b) 150 nm of PECVD SiO_2 is deposited. (c) Contact openings are etched in SiO_2 via plasma etching. (d) Antennas and contact pads are formed through deposition and liftoff of Ti/Au (10/400 nm).

APPENDIX C

Fabrication of Plasmonic Electrode Based Dipole Array Antennas on $In_{0.53}Ga_{0.47}As$

1. Pattern alignment marks

   (a) Clean the semiconductor wafer by immersing in acetone (2 min) followed by isopropanol (2 min), and rinsing with deionized water (10 sec).

   (b) Dry the sample with nitrogen and heat it on a hotplate at 115 °C for 90 sec to remove any remaining water.

   (c) Spin on HMDS at 4,000 rpm for 30 sec. Spin on Megaposit SPR 220-3.0 photoresist at 4,000 rpm for 30 sec. Pre-bake the resist on a hotplate at 115 °C for 90 sec.

   (d) Load the sample and mask plate into projection lithography stepper (GCA AutoStep 200). Align the sample and expose.

   (e) Post-bake the exposed photoresist on a hotplate at 115 °C for 90 sec.

   (f) Develop resist in AZ 300 MIF developer for 60 sec. Rinse in deionized water for 4 min. Dry the sample with nitrogen.

   (g) Place the sample in a metal evaporator (Denton SJ-20). Pump the chamber to a pressure below 2×10^{-6} Torr. Deposit Ti/Au (100/3000 Å).

   (h) Vent the chamber and remove the sample.

   (i) In order to lift-off the deposited metal, place the sample on a Teflon holder in a beaker of acetone, cover, and leave overnight. Uncover the beaker, place it in an ultrasonic agitator, and wait until all unwanted metal is removed (typically 30 sec).

2. Remove $In_{0.53}Ga_{0.47}As$ layer in all but the active region (Fig. C.1b)

   (a) Follow Steps 1.a - 1.f to mask the active region with photoresist.

(b) Place sample in a reactive ion etcher (LAM 9400). Etch the $In_{0.53}Ga_{0.47}As$ layer.

(c) Remove photoresist by soaking the sample in acetone (5 min), isopropanol (2 min), PRS 2000 (8 min, 90 °C), isopropanol (2 min).

3. Fabricate plasmonic gratings (Fig. C.1c)

(a) Clean the sample as in Steps 1.a - 1.b.

(b) Spin MicroChem 950K PMMA A4 on the sample at 4,000 rpm for 45 sec. Pre-bake the resist on a hotplate at 180 °C for 2 min.

(c) Load the sample into an electron beam lithography tool (RAITH150). Expose the plasmonic grating pattern.

(d) Develop PMMA by immersing the sample in a MIBK:IPA 1:3 mixture for 60 sec. Immediately transfer the sample to a solution of pure isopropanol for 60 sec.

(e) Rinse the sample with deionized water for 10 sec and then dry the sample with nitrogen.

(f) Load the sample into a plasma stripper (YES-CV200RFS). Descum the sample using 30 W RF power at 30 °C with a 100 sccm O_2 flow rate for 10 sec.

(g) Remove surface oxide by immersing in a HCl:H_2O 3:10 mixture for 30 sec. Immediately transfer the sample to a cascade rinse of deionized water for 4 min.

(h) Transfer the sample to a beaker of deionized water to minimize exposure to atmospheric oxygen before metal deposition.

(i) Take beaker containing the sample in deionized water to a metal evaporator (Denton SJ-20). Vent the chamber and then remove, dry, and load the sample into the chamber (these steps should be followed without interruption to prevent surface oxide formation on the sample).

(j) Pump the chamber to a pressure below 2×10^{-6} Torr. Deposit Ti/Au (30/500 Å).

(k) Vent the chamber and remove the sample.

(l) In order to lift-off the deposited metal, place the sample on a Teflon holder in a beaker of acetone, cover, and leave overnight. Uncover the beaker, place it in an ultrasonic agitator, and wait until all unwanted metal is removed (typically 30 sec).

4. Fabricate ground line (Fig. C.1d)

(a) Clean the sample as in Steps 1.a - 1.b.

(b) Spin MicroChem 950K PMMA A6 on the sample at 3,000 rpm for 45 sec. Pre-bake the resist on a hotplate at 180 °C for 2 min.

(c) Pattern the ground line by following Steps 2.c - 2.i.

(d) Pump the Denton SJ-20 to a pressure below 2×10^{-6} Torr. Deposit Ti/Au (100/1500 Å).

(e) Lift-off metal as in Steps 1.h - 1.i.

5. Deposit SiO2 passivation (Fig. C.1e)

(a) Clean the sample as in Steps 1.a - 1.b.

(b) Load the sample in a plasma-enhanced chemical vapor deposition tool (GSI PECVD). Deposit 1500 Å of SiO_2 at 200 °C.

6. Open contact vias through SiO_2 (Fig. C.1f)

(a) Pattern photoresist mask for contact vias as in Steps 1.a - 1.f.

(b) Load the sample into a reactive ion etcher (LAM 9400). Etch SiO_2 using a TCP RF power of 500 W, a Bias RF power of 100 W, 15 sccm of SF_6, 50 sccm of C_4F_8, 50 sccm He, 50 sccm of Ar for 80 sec.

(c) Remove the bulk of the photoresist by placing the sample in acetone (5 min) followed by isopropanol (2 min). Rinse in deionized water (10 sec). Dry with nitrogen.

(d) Remove the residual photoresist by loading the sample in a plasma stripper (YES-CV200RFS). Remove the photoresist using 800 W RF power at 30 °C with a 100 sccm O_2 flow rate for 5 min.

7. Fabricate antennas and bias lines (Fig. C.1g)

(a) Clean sample as in Steps 1.a - 1.b.

(b) Spin on HMDS at 1,500 rpm for 30 sec. Spin on Megaposit SPR 220-3.0 photoresist at 1,500 rpm for 30 sec. Pre-bake the resist on a hotplate at 115 °C for 90 sec.

(c) Load the sample and mask plate into projection lithography stepper (GCA AutoStep 200). Align the sample and expose.

(d) Develop resist in AZ 300 MIF developer for 60 sec. Rinse in deionized water for 4 min. Dry the sample with nitrogen.

(e) Place the sample in a metal evaporator (Denton SJ-20). Pump the chamber to a pressure below 2×10^{-6} Torr. Deposit Ti/Au (100/10,000 Å).

(f) Lift-off metal as in Steps 1.h - 1.i.

8. Package the sample

(a) Glue the edges of a 12 mm diameter hyper-hemispherical silicon lens to a 2 inch aluminum washer with 8 mm hole.

(b) Glue a PCB board with metal traces, to which one can easily solder, to the aluminum washer.

(c) Mount the fabricated plasmonic photoconductive terahertz emitter prototypes on the silicon lens using thin epoxy.

(d) Wire bond the device contact pads to a PCB board glued on the same aluminum washer.

(e) Solder wires to the metal traces on the PCB board.

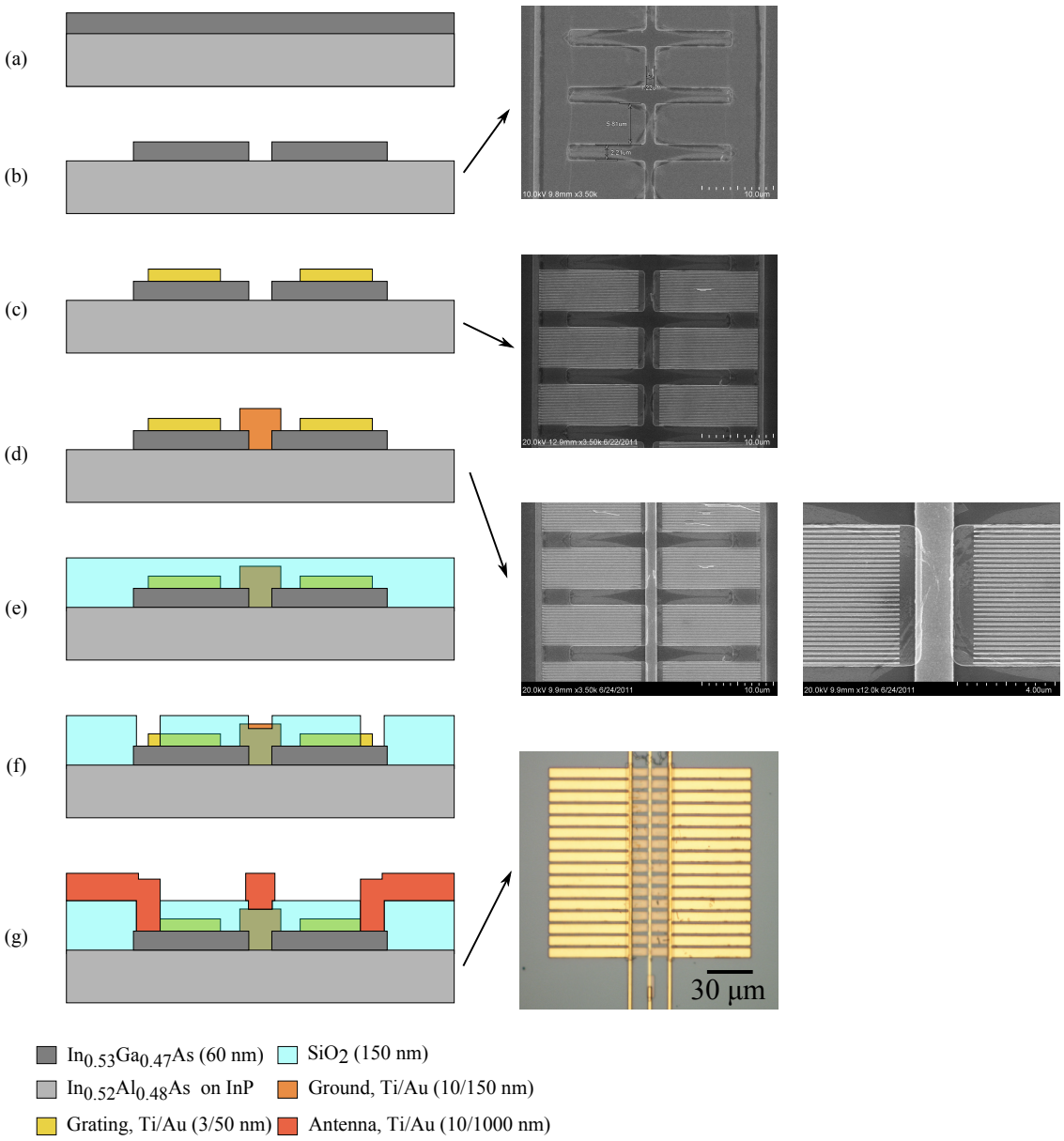

Figure C.1: Fabrication process of $In_{0.53}Ga_{0.47}As$ dipole array. Left: Process flow. Right: SEM and microscope images. (a) Begin with a wafer having a 60 nm thick $In_{0.53}Ga_{0.47}As$ layer grown on an InP substrate. (b) Etch $In_{0.53}Ga_{0.47}As$ layer in regions outside of the active area. (c) Pattern plasmonic gratings through direct-write electron beam lithography followed by deposition and lift-off of Ti/Au (3/50 nm). (d) Pattern ground line through direct-write electron beam lithography followed by deposition and lift-off of Ti/Au (10/150 nm) (e) Deposit 150 nm of PECVD SiO_2. (f) Etch contact openings in SiO_2 via plasma etching. (g) Pattern antennas and contact pads. Deposit and lift-off of Ti/Au (10/1000 nm).